

Z 4099


Prepared for:

Modelling Cyclic bar behaviour

a bottom-up modelling approach with Delft3D

Report

May, 2007

	Delft postbus 177 - 2600 MH Delft waterbouwkundig laboratorium/WL
BB	67747
WL	74099
EXPL	WL Delft Hydraulics



C 151323

Prepared for:

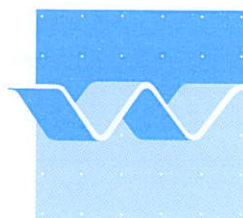
Modelling Cyclic bar behaviour

a bottom-up modelling approach with Delft3D

N. Geleynse

Traineeship Report

May, 2007



wL | delft hydraulics

Preface

Exploring the coastal system by means of the heart (Lesser et al., 2004) of the DELFT3D-modelling framework, that is, the FLOW module, contributed to the awareness that nature's complexity, yet, perhaps originating from simplicity, remains fascinating. The development of some basal understanding of existing model formulations should precede analyses of its output for user-specified conditions. Further, one can spend decades or longer on getting some idea of the intrigue and intricate nature of nature. The author hopes that the present work will serve as a small step towards further investigation of a process-based model's capability to reproduce observed cyclic bar behaviour along sandy coasts. The supervisor of my traineeship at WL|Delft Hydraulics, ir. D.J.R. Walstra, is acknowledged for offering the opportunity to study this natural feature in the final months of my study physical geography. My supervisor at Utrecht University, dr. B.G. Ruessink, is acknowledged for his effort to provide a traineeship at the institute. Further, thanks are due to prof.dr.ir. L.C. van Rijn for lending out the books of Rodi and Cebeci&Bradshaw to get some first understanding of turbulence, and to dr. C. Brière for helping me with some typical beginner Delft3D problems. The Universal Coastal Intelligence Toolkit, initiated by dr.ir. M. van Koningsveld provides a straightforward way to extract frequently needed data, such as the bathymetric data for the present study. Finally, I would like to thank my colleague-students on the 'afstudeereiland': we shared a nice time!

Preface

Contents

1	LONG-TERM NEARSHORE BAR BEHAVIOUR.....	1
1.1	LARGE-SCALE MORPHOLOGICAL DEVELOPMENTS	2
2	BAR CONSIDERATIONS	3
2.1	DEFINITION.....	3
2.2	GENERATION & MIGRATION.....	4
2.3	(MODELLING) CYCLIC MIGRATION.....	4
2.4	EXPLORING CYCLIC MIGRATION AT NOORDWIJK	6
3	DESCRIPTION OF FLUID MOTIONS.....	9
3.1	CONSERVATION LAWS	11
3.1.1	Equation of continuity (conservation of mass).....	12
3.1.2	Equations of motion (conservation of momentum)	13
3.1.2.1	3.1.2.1 Fluid accelerations	13
3.1.2.2	Fluid forces	14
3.1.2.3	Fluid momentum	16
4	DELFT3D-MODEL FORMULATIONS.....	25
4.1	SHALLOW WATER EQUATIONS.....	25
4.2	Vertical momentum equation.....	26
4.2.1	Pressure gradients.....	27
4.2.2	4.1.3 Reynolds' stresses	27
4.2.3	External momentum sources or sinks	28
4.2.4	Coriolis force.....	28
4.2.5	Transport equation.....	28

4.2.6	Turbulence closure model	29
4.3	BOUNDARY CONDITIONS.....	29
4.3.1	Offshore and lateral boundary conditions	29
4.3.2	Vertical boundary conditions.....	32
4.4	SOLUTION PROCEDURE	33
4.4.1	Hydrodynamics	33
4.4.2	Transport equation.....	34
4.5	WAVES.....	34
4.6	SEDIMENT TRANSPORT FORMULATIONS.....	35
4.6.1	TRANSPOR2004 - Delft3D	36
4.6.1.1	Bed-load transport of non-cohesive sediment (sand)	36
4.6.1.2	Suspended-load transport of non-cohesive sediment (sand)	37
4.7	MORPHODYNAMICS	38
4.8	PARAMETER SETTINGS	39
5	MODEL RESULTS	41
5.1	MORPHOLOGICAL ACCELERATION FACTOR.....	41
5.2	FIXED LAYER.....	42
5.3	TRANSVERSE BED GRADIENT FACTOR.....	43
5.4	ANALYSIS OF PREDICTED LONG-TERM BAR BEHAVIOUR.....	45
6	CONCLUSIONS & RECOMMENDATIONS.....	49
7	REFERENCES.....	50

I LONG-TERM NEARSHORE BAR BEHAVIOUR

The behaviour of a multiple bar system in the nearshore zone of a sandy coast has been studied, extensively. These studies focused on bar behaviour at time scales, ranging from hours, days and weeks (e.g., Kroon, 1994), via months and seasons (e.g., van Enckevort, 2001) to years and decades (e.g., Ruessink and Kroon, 1994; Wijnberg and Terwindt, 1995). Obviously, time- and space scales are related (figure 1), e.g., annual ‘snapshots’ of the coastal bathymetry (e.g., the Jarkus data base of yearly (since 1964) echosoundings and aerial photographs of the nearshore profile along the Holland coast (of about 115km length)) reveal the cumulative result of morphological developments on many scales (Wijnberg and Terwindt, 1995). The present study concerns bar behaviour at the yearly to decadal timescale. It is the yearly to decadal bathymetric developments that are often dominated by shore-parallel nearshore bars along uninterrupted, sandy coasts (Wijnberg and Terwindt, 1995).

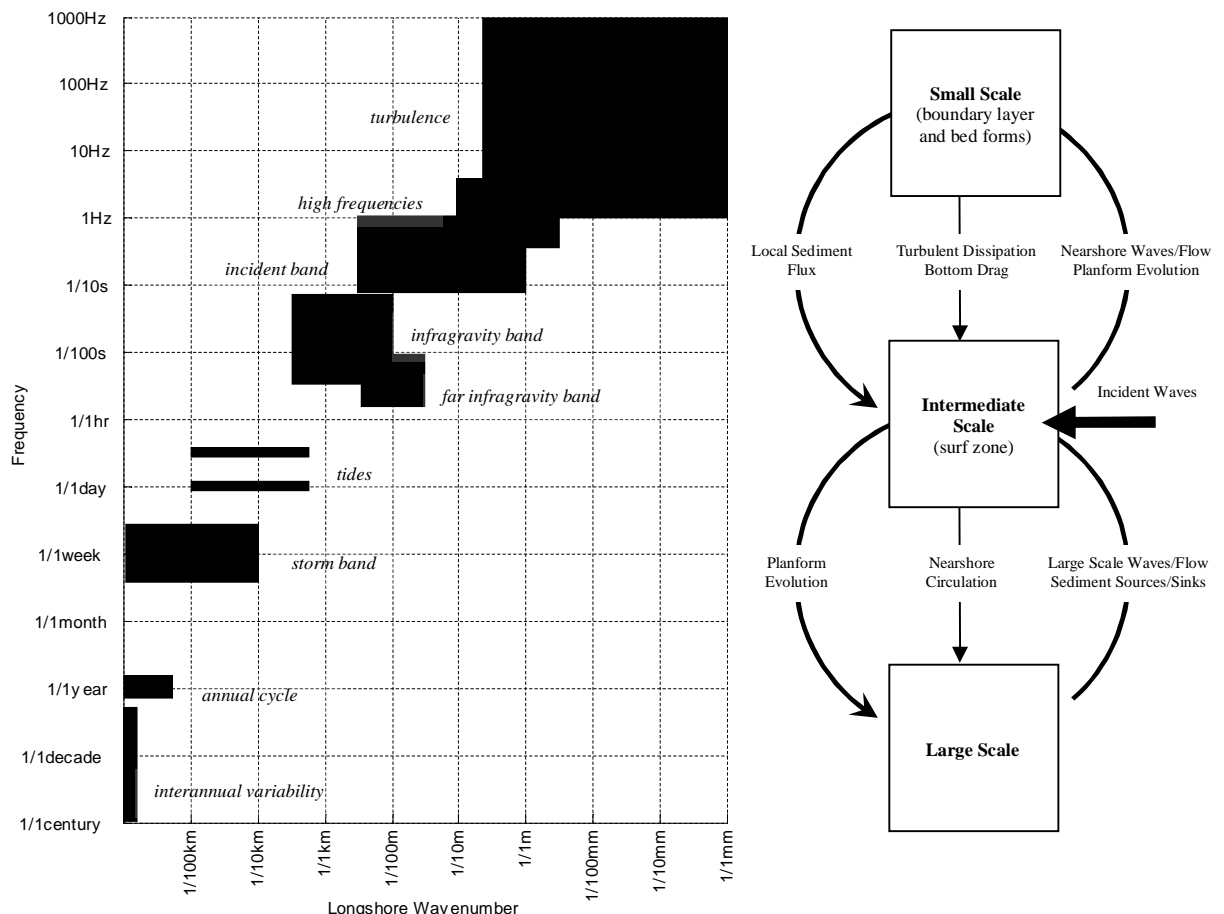


Figure 1. Coupling between space and time scales of nearshore fluid motions, shaping a coast’s morphology (left; adapted from Thornton et al., 2000). A long-term goal of nearshore research is to understand and model the transformation of surface gravity waves propagating across the continental shelf to the beach, the corresponding wave-driven circulation in the surf zone (besides the eventual impact of tidal motion and wind shear), and the resulting evolution of surf zone and beach face morphology (including feedback mechanisms). From field

experiments and numerical models it has become clear that the above-mentioned coastal system involve coupled processes at many spatial and temporal scales (*right*; adapted from Thornton et al., 2000). For example, the incident wave properties and beach profile (large-scale properties) determine the overall characteristics (e.g., surf zone width) of nearshore waves and flows (intermediate-scale properties). However, small-scale processes control the turbulent dissipation of breaking waves, bottom boundary layer and bedform processes that determine the local sediment flux (Thornton et al., 2000). Meanwhile, cross-shore- and alongshore nonuniformities in wave- and current field as well as bottom slopes cause spatial gradients in sediment fluxes, resulting in large-scale planform evolution (e.g., erosion or accretion). The development of surf zone bathymetry in turn, affects nearshore waves and currents.

1.1 LARGE-SCALE MORPHOLOGICAL DEVELOPMENTS

Little is known about the controlling variables for the morphological behavior of coastal stretches (of $O(10^0\text{-}1\text{ km})$ length) over a time span of years and decades. The concept of a large-scale coastal behaviour (LSCB) region was introduced by Wijnberg and Terwindt (1995), being an area in which the profiles show similar horizontal shifting in cross-shore direction and exhibit comparable changes in shape. They hypothesized that regions exhibiting different large-scale coastal behaviour are controlled by different (i) hydrodynamic forcings or differently balanced combinations of hydrodynamic forces, (ii) sedimentological constraints (grain size, stratigraphy) or (iii) morphological constraints (shoreline orientation, shoreface morphology, surf zone morphology), or (iv) by some combination of these factors. By using empirical eigenfunction technique and a moving window approach to effectively quantify large-scale morphological changes, Wijnberg and Terwindt (1995) identified large-scale coastal behaviour regions of several sizes (5, 15, 20, 32, 42 km) along the Holland coast, which is characterized by an alongshore varying seaward extension of the bar system, number of bars and bar spacing. They noticed that differences in the 'secondary' morphology, that is, the morphology other than the mean profile shape, such as nearshore bars, are most pronounced and that boundaries between LSCB-regions are generally quite sharp (of $O(2\text{ km})$). A marked difference in bar behaviour was found between the area northward of IJmuiden (to the Petten Seawall) and the area southward of IJmuiden (to the harbour moles of Scheveningen); bar spacing and size of the bars are generally larger in the latter area. The well-known long-term bar behaviour (with decay of the outer bar at the edge of the surf zone and generation of a new bar at the foot of the beach) is comparable for both areas. However, the length of the migrational cycle differs; in the southern area the return period is much smaller (about 4 years versus 15 years for the area northwards of IJmuiden) and the alongshore coherence in offshore bar movement seems to be larger (figure 13 in Wijnberg and Terwindt, 1995).

Thus, large-scale dynamics of multiple bar systems are characterized by their *cyclic* net offshore migration over years to decades, often being remarkably regular (van Enckevort, 2001). Although quantitative descriptions of these cyclic large-scale morphological developments have been provided, such as given above, thoroughly tested mathematical relations between morphological behaviour and controlling variables for this timescale are rather scarce. The present effort deals with the reproduction of observed cyclic bar behaviour by means of a bottom-up modelling approach, that is, the prediction of a topographic response by integrating short time-scale processes, including wave transformation, fluid motion and sediment transport. The central question is whether such an approach (hindcast) is capable of reproducing bar behaviour, and its cyclicity in particular, properly. As a case study, the coastal zone in the vicinity of Noordwijk, the Netherlands, is selected. Here, the return interval is recognized to be about 4 years, allowing model computational time not to be excessively long. Consequently, an intersite comparison cannot be made, here (see e.g., Ruessink et al., 2003). Further, bathymetric data are available that do not suffer from applied nourishments (see e.g., van Duin et al., 2004; Grunnet et al., 2004). Before treating model formulations, some theoretical background of bar definition, its generation and subsequent migration is given, first (Chapter 2). Afterwards, a description of fluid motions is provided (Chapter 3), followed by a short overview of the governing hydrodynamic equations (including the formulation for the transport of constituents) making up a Delft3D model (Chapter 4). Subsequently, model outputs are analyzed (Chapter 5). Finally, conclusions are summarized in Chapter 6.

2 BAR CONSIDERATIONS

To study bar behaviour, this chapter gives some very brief rationale behind bar definition and theoretical considerations of its generation and successive migration. Subsequently, spatial and temporal bar behaviour will be assessed for a specific site (Noordwijk) along the Holland coast, for the period 1979-1983 (one bar cycle).

2.1 DEFINITION

Nearshore bars are prominent morphological features, observed at numerous sites across the world (see e.g., Ruessink et al., 2003). Natural variability in both cross-shore and alongshore appearance of bars, and its spatial and temporal derivatives are stunning (see e.g., Table 4.1 of van Enckevort, 2001). Several bar classification schemes have been set up (e.g., based on relation between bar location and environmental setting (Wijnberg and Kroon (2002)), ultimately, to search for factors that may explain intersite differences in recognized bar behaviour. Site-specific parameters, concerning geomorphological and hydrodynamical characteristics, such as setting (open ocean versus semi-enclosed sea), beach slope, grain size, tidal range and wave climate may cause intersite differences in e.g., bar migration rate (at different temporal scales), but, as stressed by Van Enckevort (2001), it is difficult to establish certain relations. Any analysis of bar behaviour, encapsulated in bathymetric data sets, requires a proper description of spatial characteristics of the cross-shore bed profile(s). This description has often been structured as a description of geometric parameters, such as bar amplitude, bar length, bar volume, bar zone width, or water depth above the bar crest (Ruessink et al., 2003). The determination of these parameters can be performed in several ways; from (i) direct computation from bathymetric surveys (e.g., Ruessink and Kroon, 1994; figure 2) (alternatively, from remote sources), (ii) data fitting functions (e.g., Plant et al., 2001; representation of measured bathymetry by means of the superposition of two Gaussian-shaped sandbars on an underlying planar slope, complemented with a third half-Gaussian bar to incorporate steepening at the shoreline; see their figure 1), or (iii) by means of modes of a complex empirical orthogonal eigenfunction analysis, being a technique for detecting propagating wave phenomena (bars), so that dominant cross-shore coherent bar behaviour can be separated from less dominant noise, and hence, barred and nonbarred parts of a profile can be distinguished (after eventual implementation of a bar amplitude threshold; Ruessink et al., 2003).

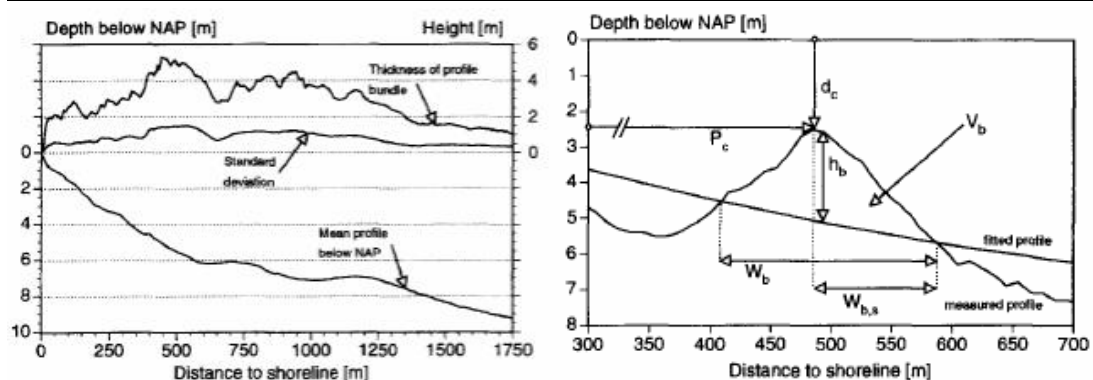


Figure 2. Left: average profile, standard deviation and thickness of the profile bundle of a cross-shore transect at Terschelling, the Netherlands (period: 1965-1993; Ruessink and Kroon, 1994). The profile bundle represents the difference between maximum and minimum measured depth values. As pointed out by Ruessink and Kroon (1994), the average profile still contains bar-like phenomena, which need to be removed for a proper morphometric analysis. This can be done by fitting a smooth profile through the mean profile. Subsequently, this fitted profile can be used to define a bar in a measured profile (right). Herein, a bar is defined as the part of the profile above the fitted line. The morphometric parameters can then be determined, such as: d_c = depth of bar crest below ordnance datum (here: NAP), P_c = bar crest position with respect to the (detrended) shoreline, h_b =

bar height (maximum deviation between measured and fitted profile), W_b = bar width, $W_{b,s}$ = width of the seaward facing side of a bar and V_b = bar volume (Ruessink and Kroon, 1994).

2.2 GENERATION & MIGRATION

Among other candidates (e.g., breakpoint mechanisms, harmonic wave overtake mechanism and mechanisms based on second-order drift velocities associated with standing infragravity waves, or those based solely on the primary orbital infragravity motions), the most suitable mechanism for explaining bar formation and migration seemed to be the extended breakpoint hypothesis (Ruessink; 1998), combining short wave flows and infragravity motions. Mean offshore-directed currents under breaking waves (undertow) transport sediment that is suspended by the orbital motion under a short wave. The asymmetry of shoaling waves causes onshore-directed sediment transport. The convergence of undertow and wave asymmetry causes sand to accumulate, hence, bars to form, just outside the surf zone. Accordingly, this bar formation mechanism is referred to as the 'breakpoint-hypothesis' (Ruessink, 1998). An extension of this hypothesis is given by Roelvink and Stive (1989) by including wave grouping induced long-wave flow. Of interest are their findings that leaving out one of the flow components in their model (i.e., excluding one of the comprising formulations of (i) undertow, (ii) short-wave velocity asymmetry and (iii) group-forced infragravity orbital motions) still resulted in bar formation, but with different bar characteristics as observed in their laboratory experiments. It is not the aim of the present study to treat possible bar formation mechanisms, extensively; for an elaborate overview, the reader is referred to e.g., Abdelrahman and Thornton (1987); Roelvink and Stive (1989); Ruessink (1998).

2.3 (MODELLING) CYCLIC MIGRATION

As mentioned before, long-term sandbar behaviour often has a cyclic offshore-directed character. A bar cycle comprises the generation of a bar near the shoreline, followed by its net offshore migration through the surf zone, and its final disappearance at the seaward margin of the nearshore. Bar decay may be seen as the trigger for the onset of net offshore migration of the next shoreward-located bar and the formation of a new bar near the waterline. The study of Wijnberg & Terwindt (1995) points at this type of bar behaviour to be alongshore coherent for alongshore lengths of more than 10 km. Accordingly, observed bar behaviour reflects cross-shore oriented bar variability, thus, is not the result of alongshore propagating shore oblique bars (Ruessink et al., 2003).

To develop a predictive understanding of the variability of a distinct morphologic feature (figure 3), such as the long-term (yearly) cyclic character of bars, models can be developed that integrate short time-scale processes, including wave transformation, fluid motion and sediment transport. By aggregation of small- to larger-scale processes, a bottom-up modelling approach is followed. Herein, a wave-, current- and wind field are typically imposed on an initial morphology, and a final morphology is predicted using sediment transport formulae. If the final morphology can be well-predicted using this approach, the morphology is said to exhibit forced behaviour (Thornton et al., 2000). However, the predictive skill of these models is uncertain on large temporal (and spatial) scales. Moreover, several studies indicate that such a forced behaviour is commonly not fulfilled for (Plant et al., 2001; Ruessink et al., 2003). For that reason, a top-down modelling approach can be followed.

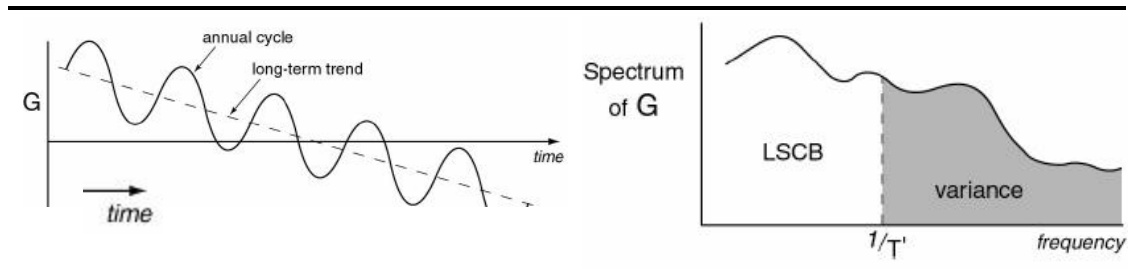


Figure 3. Left: Synthetic coastal signal (G) variations (e.g., beach behaviour), viewed as the superposition of a deterministic annual cycle and an underlying long-term trend. Predicting the long-term behaviour would be specified by the trend, with variance of the annual signal making up the confidence limit (cf. regionalized variable theory; Burroughs & McDonnell, 1998). In other words, and more realistic, since nearshore variability occurs over all spatial and temporal scales (with significant energy at the longest scales), prediction of LSCB is made beyond a certain temporal (or spatial) scale (T') with the shorter period (or length) fluctuations considered to be variance of the prediction (Thornton et al., 2000; *right*). Models for nearshore processes are typically based on physical laws expressing conservation of mass, momentum and energy (Chapter 3). At small and intermediate scales (figure 1), understanding the nearshore implies the understanding of both its fluid and sediment components (Thornton et al., 2000). At the longer time scales of Large Scale Coastal Behaviour (LSCB; Section 1.1), emergent variables based on a hierarchy of time scales may dominate nearshore processes (Thornton et al., 2000). For these longer time scales of LSCB, the primary tool is conservation of sediment mass, because of the bathymetry being the main variable of interest. For example, annual cycles in sand bar location may have no LSCB impact (meaning that they only deliver variance), whereas net alongshore transport gradients, dune overtopping or offshore losses can lead to important LSCB signals (Thornton et al., 2000). In other words, if mass conservation is implemented via a box model, fluxes within that box may be neglected, whereas fluxes across box boundaries may control long term behaviour (Thornton et al., 2000). Forcing of large scale nearshore variability can arise from several sources, including (i) external factors (wave-, current- and wind climates), (ii) nonlinear interactions within these external factors, and (iii) internal (to the system) factors. (i) Directly forced response is the result of forcing energy at the same frequency, e.g., slow erosion of the beach due to a slow increase in wave energy (Thornton et al., 2000). (ii) Nonlinear interactions may transfer energy of the forcing spectrum from high frequencies to LSCB, e.g., increased suspended sediment loads under winter storm waves might tend to be carried preferentially offshore by the undertow, while summer conditions might drive only a weak onshore transport, resulting in a net sediment loss (Thornton et al., 2000). (iii) Spontaneous generation of LSCB variance (free behaviour: see text) is caused by instabilities and feedback within the nearshore system, e.g., generation of ripples on an initially smooth bed (generated by an instability and feedback between a perturbation in bed roughness that causes a disturbance to the flow and sediment transport that, in turn, reinforces the perturbation (Thornton et al., 2000)). In terms of sandbars: these may be generated by, and may induce the onset of wave breaking.

It is suggested that the nearshore response is sensitive to initial perturbations in the bed profile and that morphologic feedback to the wave- and current field can be strong (e.g., a decaying outer bar results in a larger water depth, so that wave breaking shifts in onshore direction). As such, morphological developments do not depend solely on the instantaneous small-scale processes; they also incorporate some degree of time history in profile configuration and may be driven by instabilities of the well-known coupled fluid-morphology system (Thornton et al., 2000). Such a system is thought to exhibit so-called free behaviour, in which the predictability time scales are limited by the strength of the nonlinear feedback, or growth rate of an instability (Thornton et al., 2000). Although only circumstantial evidence is present, the nearshore system is thought to have the key characteristics to exhibit free behaviour (Ruessink et al., 2003): “the nearshore system is highly dimensional and strongly nonlinear, it receives a continuous, stochastically forced input of energy which is dissipated within the system, and it contains morphologic feedback, as changes in depth gives rise to changes in waves and currents”. The findings of Plant et al. (2001) also point at the importance of feedback mechanisms associated with surf zone sandbar response. From their analysis it became clear that bar migration appears to be associated with a stabilizing feedback mechanism, which drives bar crests toward equilibrium at the wave breakpoint. Of interest are their observed differences from the classical breakpoint models, namely: (i) migration of existing bars accounts for most of the variability of the system (not the formation of new bars), (ii) though the breakpoint is not usually viewed as a sharply defined location under random wave conditions, the value of the commonly used ratio of wave height to water depth, (separating onshore and offshore migration in this study) could be sharply defined and (iii) bars may never reach equilibrium.

2.4 EXPLORING CYCLIC MIGRATION AT NOORDWIJK

The degree of alongshore coherence in temporal changes in profile characteristics describing the large-scale morphological behaviour (Wijnberg and Terwindt, 1995) is investigated for the present study area (figure 4).

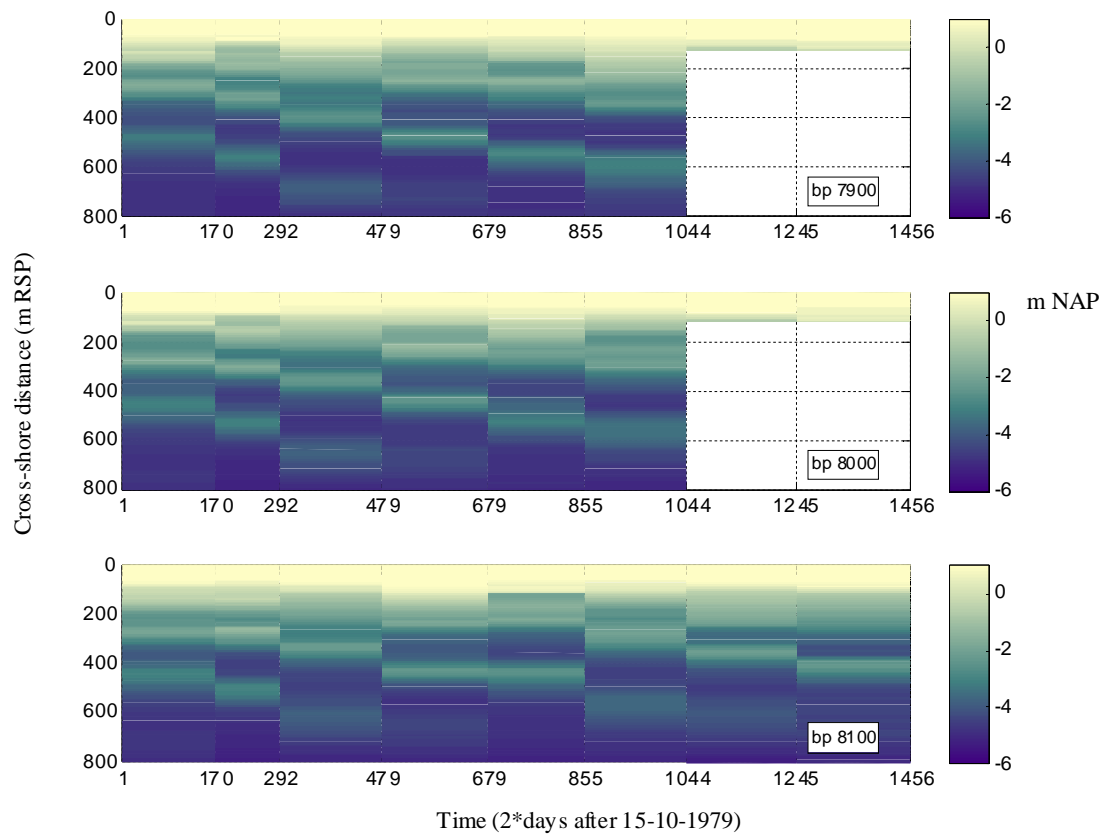


Figure 4. Timestacks for three transects (beachpoles 7900, 8000 and 8100 near Noordwijk), showing a bar migration cycle within a time interval of approximately 4 years. The alongshore coherence in observed cyclic bar behaviour on a km-scale can be clearly recognized, so that, eventually, the need for alongshore averaging of individual transects vanishes. Although an alongshore averaging procedure may represent the mean-behaviour of the area-mean cross-shore profile more properly, eventual (local) characteristic bar geometry may be represented somewhat weakly. Ultimately, application of a full 3D-model (or a 2DV/2DH-model, but with less certainty, presumably) may give insight in the effect of alongshore morphological inhomogeneities on cross-shore bar behaviour.

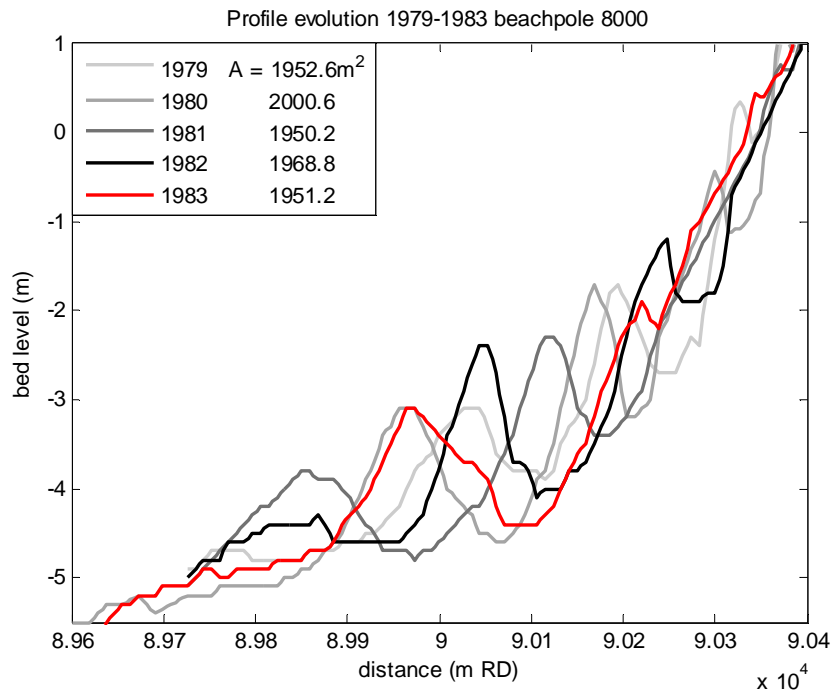


Figure 5. Temporal cross-shore bar behaviour and computed profile volumes ($x_{RD} = [89750:90400]$ m) at beachpole 8000, for each year within ($t = [1979:1983]$). See next page for more info. Profile volumes are quite constant trough time, possibly inferring that the net seaward-directed bar migration has a dominant cross-shore oriented origin. It is emphasized here, that the bed profiles shown here must be treated carefully, because of possible effects of (i) different measurement dates of higher and lower part of the profile, as well as seasonal bias in profile sampling due to a varying time interval between two successive profile soundings (here between 8 and 11 months), (ii) application of a linear interpolation technique (e.g., notice the absence of an intertidal bar in the upper part of the profile of 1981, due to missing data) and (iii) ordinary measurement inaccuracies. Although the net seaward migration of the bar system is unequivocally clear, it must be realized that the low temporal resolution of the field data hampers an in-depth comparison with usual high resolution model predictions (i.e. yearly measured profiles form only ‘snapshots’ of examined bar cycle).

For the present study, a profile model is employed, since cyclic bar behaviour is likely to be, in essence, a cross-shore redistribution of sand (Wijnberg, 1995; see computed profile volumes in figure 5). The aforementioned alongshore coherence in temporal variations in bar morphology (figure 4), such as, for instance, is recognized for the region (roughly) extending from the harbour moles of IJmuiden to Scheveningen (km 58-98 relative to Den Helder, Netherlands) for the period 1963-1990 (Wijnberg and Terwindt, 1995) may offer the possibility to successfully reproduce the medium-term (of $O(10^{0-1})$ yr) cyclic bar behaviour with a profile model.

Presumably, the effect of offshore wave forcing on cross-shore bar migration depends on the time span (eq [4.8] of Van Enckevort, 2001). In the study of Plant et al. (1999), yearly bar migration rates were found to vary independently of the yearly averaged wave climate. For example, net yearly offshore bar migration rate changes during the lifetime of a bar (as can be inferred from figure 5), while the yearly averaged wave climate remains virtually constant (Ruessink and Kroon, 1994), suggesting that the yearly offshore bar migration rate is essentially controlled by local (referring to the morphology of the bar itself) and non-local (referring to the morphology of seaward located bars) morphological feedback mechanisms (Ruessink and Terwindt, 2000; see Section 2.3). It is, however, largely unknown at which time scale the effect of direct wave forcing becomes subordinate to the effect of feedback mechanisms.

To further investigate the potential capability of a profile model to reproduce cyclic bar migration, a CEOF analysis (Ruessink et al., 2003) is performed (figure 6).

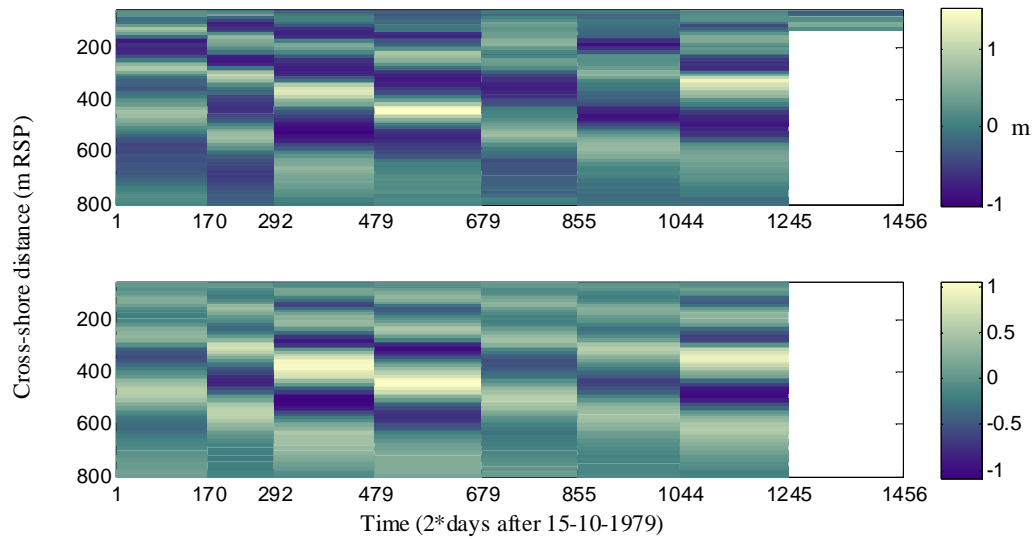


Figure 6. Results of eigenvector analysis for beachpole 8000 at Noordwijk. *Upper panel:* perturbations relative to mean (1979-1987) (barless) cross-shore profile, *lower panel:* first eigenvector (explaining 71.8% of the total variance), representing the net seaward bar migration, clearly.

In agreement with the results of Ruessink et al. (2003), the first complex mode (depicted in lower panel of figure 6) represents highest percentage of total depth variance. It describes the long-term offshore progressive behaviour clearly, thereby allowing an objective separation of the barred part from the nonbarred parts of the profile to be made, thereby supporting the present profile modelling approach.

3 DESCRIPTION OF FLUID MOTIONS

A material's motion has been studied for decades, or even centuries, now. Yet, to describe these motions remains a challenging difficulty; e.g., even though observed random (or probably better: irregular), unsteady and three-dimensional fluid flow behaviour, known as 'turbulence', is an everyday experience, turbulent fluid motion and its associated heat and mass-transfer phenomena are still difficult to describe, and hence, to predict theoretically. The starting-point of a mathematical description of motions of any material is formed by balance equations, to arrive at a closed system of equations, ultimately. Meanwhile, models often incorporate assumption upon assumption regarding fluid and flow field properties, so that solutions for the specific problem of interest crystallize. As pointed out by Cramer (2004), the general development of the set of governing equations for *any* material involves five steps:

- I. Generation of balance equations representing fundamental physical laws, holding for all materials, e.g., solids, fluids, visco-elastic materials, and rigid bodies. In the mechanical world, these equations, usually applied in integral form to a finite mass of material, include laws expressing conservation of mass, (linear) momenta and energy (some form of the second law of thermodynamics).
- II. Conversion of the integral equations (I) to a 'local' form, which then casts the conservation laws in the form of partial differential equations (e.g., all of the dependent variables; velocity vector, pressure, density and temperature, are functions of all independent variables; position vector and time).
- III. Specification of the material response, necessary to close the system, because the former equations cannot be solved in a general way for the details of the material motion. The mathematical conditions are usually referred to as the constitutive relations (e.g., stress - rate of strain (deformation) relations).
- IV. Combination of the constitutive relations with the local form of the balance equations, yielding the so-called field equations which are the differential equations governing the material of interest.
- V. Definition of physical conditions and the shock jump (or Rankine-Hugoniot) conditions, the latter governing the motion of propagating discontinuities. This is achieved by returning to the integral balance laws, with the possible presence of discontinuities in basic variables such as e.g., the stress, heat flux, particle velocity, internal energy taken into account. The physical boundary conditions are obtained by considering only 'material' interfaces, i.e., those which comprise material boundaries. The general form of the Rankine-Hugoniot jump conditions are obtained by restricting attention to surfaces of discontinuity which propagate relative to the material. Finally, material-specific conditions may also need to be incorporated.

In case of the considered material to be a so-called Navier-Stokes fluid (e.g., a Newtonian fluid), the above-listed general, but complete set of physical conditions describing a material's motion is known as the Navier-Stokes equations. As stressed by Mei (2002), the full set of Navier-Stokes equations is so complex that it is unrealistic and unrevealing to search for the most general solutions. Instead, systematic approximations for certain specific circumstances can be obtained by means of scale analyses, wherein dimensionless parameters (e.g., the Strouhal number, $St \sim \text{local acceleration/convective acceleration}$, Froude number, $Fr^2 \sim \text{inertia/body force}$ and Reynolds number, $Re \sim \text{inertia/viscous force}$) capture the relative importance of each term making up the full equations. Generally speaking, the Navier-Stokes equations establish that changes in (mean) momentum of fluid particles are the product of changes in pressure and dissipative viscous forces (originating in molecular interactions) acting inside the fluid. Thus, the equations are a dynamical statement of the balance of forces acting at any given region of the fluid. Besides their useage for modelling ocean currents and weather systems, they are also used in e.g., the design of aircraft, the study of blood flow and the analysis of the effects of pollution. Since they are differential equations, unlike algebraic equations, they do not seek to establish a relation among the variables of interest (e.g., velocity and pressure), rather they establish relations among the rates of change, or fluxes of these quantities. In mathematical terms, these rates correspond to their derivatives. For example, in case of an ideal (i.e.,

incompressible, inviscid and irrotational) fluid, the Navier-Stokes equations state that acceleration is proportional to the derivative of internal pressure (Euler equations). It is only in few cases that the Navier-Stokes equations can be solved exactly; consequently, solutions of the Navier-Stokes equations for a specific physical problem are often found using numerical methods (collectively referred to as Computational Fluid Dynamics).

To develop some first understanding of the overall structure of equations describing fluid substances, such as gases and liquids, and the connection of that structure to more fundamental physical principles, eqs. [1] give some general form of the Navier-Stokes equations in a Cartesian coordinate system with directions (i,j,k) = (x,y,z) for the three components of the fluid velocity vector (NASA, 2006):

$$\text{Continuity:} \quad \frac{\partial \rho}{\partial t} + \frac{\partial(\rho U)}{\partial x} + \frac{\partial(\rho V)}{\partial y} + \frac{\partial(\rho W)}{\partial z} \quad [1a]$$

Momenta:

$$\begin{aligned} x: \quad & \frac{\partial(\rho U)}{\partial t} + \frac{\partial(\rho U^2)}{\partial x} + \frac{\partial(\rho UV)}{\partial y} + \frac{\partial(\rho UW)}{\partial z} = -\frac{\partial P}{\partial x} + \frac{1}{\text{Re}_r} \left(\frac{\partial \tau_{xx}}{\partial x} + \frac{\partial \tau_{xy}}{\partial y} + \frac{\partial \tau_{xz}}{\partial z} \right) \\ y: \quad & \frac{\partial(\rho V)}{\partial t} + \frac{\partial(\rho UV)}{\partial x} + \frac{\partial(\rho V^2)}{\partial y} + \frac{\partial(\rho VW)}{\partial z} = -\frac{\partial P}{\partial y} + \frac{1}{\text{Re}_r} \left(\frac{\partial \tau_{xy}}{\partial x} + \frac{\partial \tau_{yy}}{\partial y} + \frac{\partial \tau_{yz}}{\partial z} \right) \\ z: \quad & \frac{\partial(\rho W)}{\partial t} + \frac{\partial(\rho UW)}{\partial x} + \frac{\partial(\rho VW)}{\partial y} + \frac{\partial(\rho W^2)}{\partial z} = -\frac{\partial P}{\partial z} + \frac{1}{\text{Re}_r} \left(\frac{\partial \tau_{xz}}{\partial x} + \frac{\partial \tau_{yz}}{\partial y} + \frac{\partial \tau_{zz}}{\partial z} \right) \end{aligned} \quad [1b]$$

Energy:

$$\begin{aligned} & \frac{\partial(\rho E_T)}{\partial t} + \frac{\partial(\rho U E_T)}{\partial x} + \frac{\partial(\rho V E_T)}{\partial y} + \frac{\partial(\rho W E_T)}{\partial z} = -\frac{\partial(\rho U P)}{\partial x} - \frac{\partial(\rho V P)}{\partial y} - \frac{\partial(\rho W P)}{\partial z} - \frac{1}{\text{Re}_r \text{Pr}_r} \left(\frac{\partial q_x}{\partial x} + \frac{\partial q_y}{\partial y} + \frac{\partial q_z}{\partial z} \right) \\ & + \frac{1}{\text{Re}_r} \left[\frac{\partial}{\partial x} (U \tau_{xx} + V \tau_{xy} + W \tau_{xz}) + \frac{\partial}{\partial y} (U \tau_{xy} + V \tau_{yy} + W \tau_{yz}) + \frac{\partial}{\partial z} (U \tau_{xz} + V \tau_{yz} + W \tau_{zz}) \right] \end{aligned} \quad [1c]$$

where (instantaneous) velocity components (U, V, W), time (t), fluid density (ρ), total energy (E_T), pressure (P), stress (τ), heat flux (q), and the similarity parameters: Reynolds number ($\text{Re}_r \sim \text{inertia/viscous force}$) and Prandtl number ($\text{Pr}_r \sim \text{momentum diffusivity/thermal diffusivity}$). The terms on the left hand side of the momentum equations are called the advection (or: convection) terms of the equations. Advection is a physical process that occurs in a fluid flow in which some property is transported by the ordered motion of the flow. The terms on the right hand side of the momentum equation that are multiplied by the inverse Reynolds number are called the diffusion terms. Diffusion is a physical process that occurs in a fluid flow in which some property is transported by the random motion of the molecules of the fluid. Diffusion is related to the stress tensor and to the viscosity of the fluid. Turbulence and the generation of boundary layers are the result of diffusion in the flow. The well-known Euler equations contain only the advection terms of the Navier-Stokes equations and cannot, therefore, model boundary layers (Cebeci and Bradshaw, 1977; Uijtewaald, 2006).

It can be noticed that the dependent variables appear in each equation [1a-c]; to solve a flow problem, all five equations have to be solved simultaneously, being the reason for calling [1] a coupled system of equations. There is actually some other equation required to solve this system, because only five equations have been shown, whereas six unknowns are incorporated. An equation of state relates the pressure, temperature and density of the fluid; obviously, if the fluid is assumed incompressible, the need for such an equation vanishes. Further, all terms of the stress tensor need to be specified. In Computational Fluid Dynamics, the stress tensor terms are often approximated by a turbulence model.

In the following, some basic principles underlying the Navier-Stokes equations will be treated more specifically, being necessary to study fluid motions, properly. Afterwards, the implementation of these equations in the Delft3D package (flow module) will be discussed, briefly.

3.1 CONSERVATION LAWS

As afore-mentioned (I), to derive the Navier-stokes equations, it is convenient to consider a finite arbitrary volume, called a control volume (figure 7), over which the principles of conservation of mass, (linear) momentum and energy can be applied. This control volume can remain fixed in space (Eulerian method; observation of motion of fluid particles as they pass fixed points in space (streamline)) or can move with the fluid (Lagrangian approach; observing given fluid particles as they move through space (fluid particle path)); see Section 4.2 on GLM reference frame).

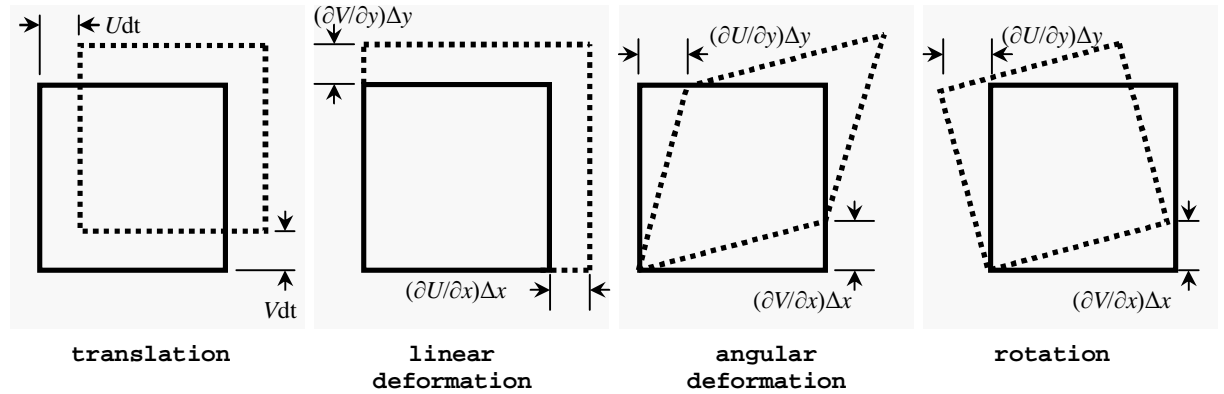


Figure 7. Basic four modes of deformation for (or displacement in) an elementary fluid volume (with size Δx , Δy and Δz) in the x-y plane, being the result of spatial variations in velocity (adapted from Van Rijn, 1994). Linear and angular deformation involve a change in shape of the fluid element, that is, a fluid compression (through diffusion-dispersion), whereby heat is generated and mechanical energy is dissipated, resulting from viscous action in the fluid. Contrarily, rotation (through diffusion-dispersion) and translation (through advection) involve a deformation without a change in shape of the fluid element.

In its most general form, a conservation law states that the rate of change of an extensive property (L) defined over a control volume (volume Ω and bounding surface $\partial\Omega$) must equal what is lost through the boundaries of the volume carried out by the moving fluid plus what is created (consumed) by sources (sinks) inside the control volume (Q). In other words (Cramer, 2004):

$$\frac{d}{dt} \int_{\Omega} L \, d\Omega = - \int_{\partial\Omega} L \mathbf{v} \cdot \mathbf{n} \, d\Omega + \int_{\Omega} Q \, d\Omega \quad [2a]$$

where \mathbf{v} is the velocity vector, \mathbf{n} is the unit outward normal to the surface of the control volume; \mathbf{n} is the most natural way to represent the orientation of the surface: $\mathbf{n} \equiv \nabla F / |\nabla F|$, where $F(\mathbf{x}, t) \equiv 0$ is the mathematical representation of the surface, which can be moving or stationary.

If the control volume is fixed in space (thus, the volume Ω and its bounding surface $\partial\Omega$ are chosen such that the integrals are always over the same mass particles), by Gauss' theorem (between brackets below), [2a] reads:

$$\frac{d}{dt} \int_{\Omega} L \, d\Omega = - \int_{\Omega} \nabla \cdot (L \mathbf{v}) \, d\Omega + \int_{\Omega} Q \, d\Omega \quad \left(\iiint_{\Omega} \nabla \cdot \mathbf{v} \, d\Omega = \iint_{\partial\Omega} \mathbf{v} \cdot \mathbf{n} \, d\Omega \right) \quad [2b]$$

which can be rewritten, yielding:

$$\frac{d}{dt} \int_{\Omega} L \, d\Omega = - \int_{\Omega} (\nabla \cdot (L \mathbf{v}) - Q) \, d\Omega \quad [2c]$$

Since Ω is invariant in time the d/dt and $\int_{\Omega} d\Omega$ operators vanish, and, as [2c] is valid for all domains, the integral can be dropped, additionally. Assuming no sources or sinks to be present in the flow ($Q = 0$), [2c] reads:

$$\frac{\partial}{\partial t} L + \nabla \cdot (L \mathbf{v}) = 0 \quad [2d]$$

3.1.1 Equation of continuity (conservation of mass)

Conservation of mass is a fundamental concept of physics; within some study domain, the amount of mass remains constant, implying that mass is neither created nor destroyed. The mass of any object is simply the product of the volume that the object occupies and the density of the object. For a fluid (a liquid or a gas), the density, volume and shape of the object can all change within the domain with time. In figure 8, the mass flow rate in and out of an elementary control volume of size (dx, dy, dz) is shown. The mass flow rate out of the region (B), in the positive x-direction, is given by the mass flow rate in (A) plus the rate of change of mass flow rate over dx (Van Rijn, 1994):

$$\rho U dy dz + \frac{\partial}{\partial x}(\rho U dy dz) dx \quad [3]$$

where higher-order terms (from Taylor series) have been neglected (i.e. the control volume is assumed to be infinitely small).

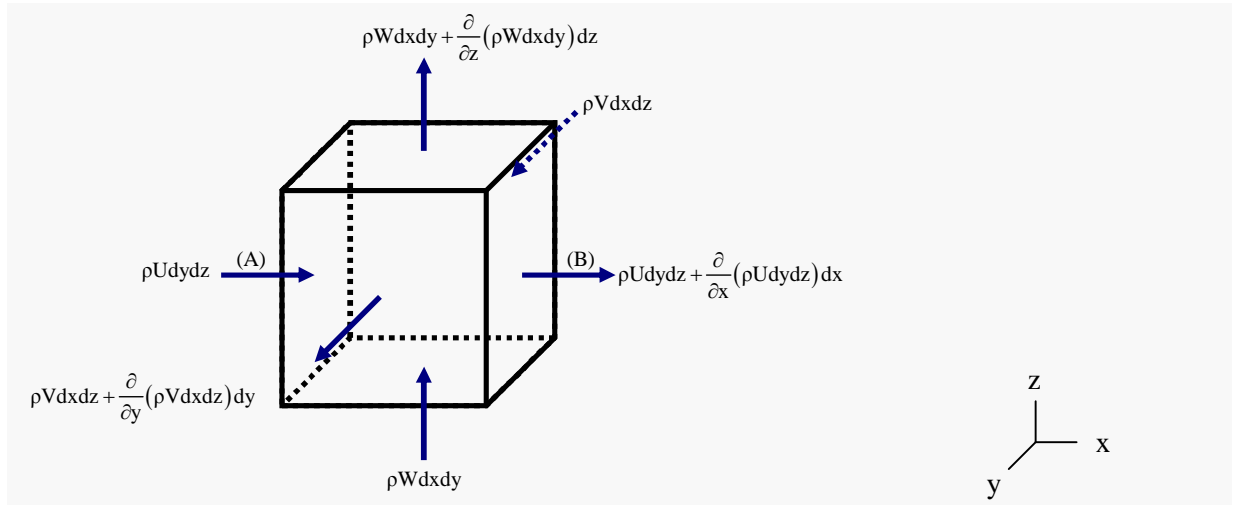


Figure 8. Mass flow rate in and out of an elementary control volume.

The net inflow of mass in the positive x-direction per unit time is the difference between (A) and (B):

$$-\frac{\partial}{\partial x}(\rho U dy dz) dx \quad [4a]$$

Notice the negative sign representing the net character (i.e. if $B > A$ then the outcome of [4a] is negative $[-(B-A)]$ with $B-A > 0$, which means that the net inflow of mass in the *positive* x-direction is negative).

Similarly, the net rate of mass flow into the region in the positive y- and positive z- direction read as:

$$-\frac{\partial}{\partial y}(\rho U dx dz) dy \quad -\frac{\partial}{\partial z}(\rho U dx dy) dz \quad [4b-c]$$

The rate of increase of mass in the region (figure 8), if not zero, is:

$$\frac{\partial}{\partial t}(\rho dx dy dz) \quad [5]$$

and thus, one can write:

$$-\frac{\partial}{\partial x}(\rho U dy dz) dx - \frac{\partial}{\partial y}(\rho V dz dx) dy - \frac{\partial}{\partial z}(\rho W dx dy) dz = \frac{\partial}{\partial t}(\rho dx dy dz) \quad [6a]$$

Since dy and dz do not vary with x ; dx and dz do not vary with y ; dx and dy do not vary with z and dx, dy and dz do not vary with t , one is allowed to divide [6a] by the volume of the considered region $(dx dy dz)$, resulting in:

$$\frac{\partial(\rho U)}{\partial x} + \frac{\partial(\rho V)}{\partial y} + \frac{\partial(\rho W)}{\partial z} = -\frac{\partial \rho}{\partial t}$$

[6b]

Using the nabla operator for the divergence of the (instantaneous) velocity vector (\mathbf{v}), [6b] can be rewritten as (cf. [2d]):

$$\begin{aligned}\frac{\partial \rho}{\partial t} + \nabla \cdot (\rho \mathbf{v}) &= 0 \\ \frac{\partial \rho}{\partial t} + \rho \nabla \cdot \mathbf{v} + \mathbf{v} \cdot \nabla \rho &= 0 \\ \frac{D\rho}{Dt} + \rho \nabla \cdot \mathbf{v} &= 0\end{aligned}\tag{6c}$$

where ρ is the mass density. In the final expression for a compressible fluid, the substantial derivative appears. The substantial (or material or particle) derivative is the derivative following a moving fluid parcel (Lagrangian approach), in contrast to the spatial derivative, which is the derivative of a field with respect to a fixed position in space (Eulerian approach). Here, the specific term 'field' stands for the field view, in which the dependent variables (velocities, pressures (density) and temperatures) are taken to be piecewise continuous functions of space and time. Basically, the substantial derivative is given by:

$$\frac{D(*)}{Dt} \equiv \frac{\partial(*)}{\partial t} + \mathbf{v} \cdot \nabla(*)$$

where $(*)$ can denote any quantity, including tensors, vectors and scalars. Thus, this equation simply expresses the time rate of change of $(*)$ as experienced by a material particle; the first term on the right-hand side of the equation is the ordinary Eulerian derivative, denoting the change of a property at a fixed point with respect to time (also known as the local acceleration, being absent in steady flows); the second term represents the changes brought about the moving fluid, which is known as advection or convection (the latter terms are often used interchangeably), being absent in uniform flows.

Assuming the fluid to be incompressible ($D\rho/Dt = 0$), [6c] takes on a simplified form:

$$\nabla \cdot \mathbf{v} = 0 \quad \left(= \frac{\partial U}{\partial x} + \frac{\partial V}{\partial y} + \frac{\partial W}{\partial z} = 0 \right)\tag{6d}$$

3.1.2 Equations of motion (conservation of momentum)

Knowledge of the afore-mentioned mass flow rate can be used to determine the forces on an object (e.g., forces on an aircraft, water body, etc.), because by Newton's second law of motion, these are directly related to the change in a fluid's momentum with time. Since momentum is defined to be the mass times the velocity of an object, one can expect the hydrodynamic (or, alternatively, the aerodynamic-) forces to depend on the mass flow rate past an object. Thus, the starting-point of the equations expressing conservation of momentum is formed by the derivation of general expressions for a fluid's acceleration and forces acting on it.

3.1.2.1 3.1.2.1 Fluid accelerations

Fluid velocity may vary with position and time, that is,

$$\mathbf{v} = f(\mathbf{r}, t) = \frac{d\mathbf{r}}{dt}\tag{7}$$

in which: \mathbf{r} = position vector with components x, y, z
 \mathbf{v} = fluid velocity vector with components U, V, W

The three velocity components in [7] are also functions of position and time:

$$U = \frac{dx}{dt} = U(x, y, z, t) \quad V = \frac{dy}{dt} = V(x, y, z, t) \quad W = \frac{dz}{dt} = W(x, y, z, t)\tag{8a-c}$$

Since the velocity of a fluid element is a function of both position and time, for the x-, y- and z-component the following expressions can be written, respectively:

$$\begin{aligned} dV &= \frac{\partial V}{\partial x} dx + \frac{\partial V}{\partial y} dy + \frac{\partial V}{\partial z} dz + \frac{\partial V}{\partial t} dt \\ dU &= \frac{\partial U}{\partial x} dx + \frac{\partial U}{\partial y} dy + \frac{\partial U}{\partial z} dz + \frac{\partial U}{\partial t} dt \\ dW &= \frac{\partial W}{\partial x} dx + \frac{\partial W}{\partial y} dy + \frac{\partial W}{\partial z} dz + \frac{\partial W}{\partial t} dt \end{aligned} \quad [9a-c]$$

Subsequently, the accelerations in x-, y- and z-direction can be defined, respectively:

$$\begin{aligned} a_x &= \frac{dU}{dt} = \frac{\partial U}{\partial x} \frac{dx}{dt} + \frac{\partial U}{\partial y} \frac{dy}{dt} + \frac{\partial U}{\partial z} \frac{dz}{dt} + \frac{\partial U}{\partial t} \quad \left(= \frac{\partial U}{\partial x} U + \frac{\partial U}{\partial y} V + \frac{\partial U}{\partial z} W + \frac{\partial U}{\partial t} \right) \\ a_y &= \frac{dV}{dt} = \frac{\partial V}{\partial x} \frac{dx}{dt} + \frac{\partial V}{\partial y} \frac{dy}{dt} + \frac{\partial V}{\partial z} \frac{dz}{dt} + \frac{\partial V}{\partial t} \quad \left(= \frac{\partial V}{\partial x} U + \frac{\partial V}{\partial y} V + \frac{\partial V}{\partial z} W + \frac{\partial V}{\partial t} \right) \\ a_z &= \frac{dW}{dt} = \frac{\partial W}{\partial x} \frac{dx}{dt} + \frac{\partial W}{\partial y} \frac{dy}{dt} + \frac{\partial W}{\partial z} \frac{dz}{dt} + \frac{\partial W}{\partial t} \quad \left(= \frac{\partial W}{\partial x} U + \frac{\partial W}{\partial y} V + \frac{\partial W}{\partial z} W + \frac{\partial W}{\partial t} \right) \end{aligned} \quad [10a-c]$$

where the particle derivative can be recognized.

Obviously, in vector form, the acceleration of a fluid particle is given by:

$$\mathbf{a} = \frac{d\mathbf{v}}{dt} = U \frac{\partial \mathbf{v}}{\partial x} + V \frac{\partial \mathbf{v}}{\partial y} + W \frac{\partial \mathbf{v}}{\partial z} + \frac{\partial \mathbf{v}}{\partial t} \quad \left(= (\mathbf{v} \cdot \nabla) + \frac{\partial \mathbf{v}}{\partial t} \right) \quad [10d]$$

3.1.2.2 Fluid forces

Two general types of forces acting on a fluid element can be distinguished: (i) forces on the volume or mass of a fluid element (body forces) and (ii) forces acting on the surface of a fluid element (surface forces). Surface forces can be further decomposed into forces normal to the surface (pressure) and forces tangential to the surface (shear). In case of an inviscid fluid, the surface stresses are only normal stresses due to pressure (figure 9). The body force is also known as the long-range force (Mei, 2001), because the origin of the force is far away from the zone of interest. The strength of such forces (e.g., gravity or Coriolis force) varies very slowly, and acts uniformly on all parts of a fluid parcel, so that the total force is proportional to the volume of fluid. Contrarily, surface forces are commonly called short-range forces; these forces originate in molecular interactions, and, therefore, decrease rapidly with increasing distance between interacting elements. A surface force is only appreciable when fluid elements are in contact, meaning that it exists only on the boundary. Surface force per unit area is called stress, which depends on time, location and on the orientation of the surface element.

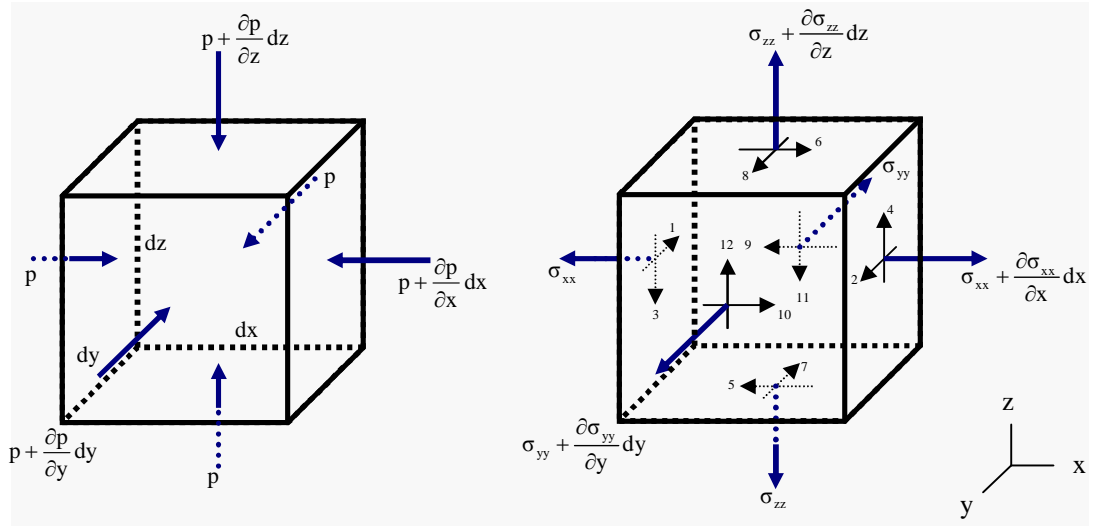


Figure 9. Left: Normal stresses due to pressure in an inviscid fluid. Right: Additional tangential (shear) stresses (numbers) in a viscous fluid. Note that σ_{xx} , σ_{yy} and σ_{zz} not only represent normal stresses due to pressure; they also contain a contribution from the fluid's viscosity. For example, the shear stresses acting on the (dy-dz)-plane are (1) τ_{yx} ($= \sigma_{yx}$) and (3) τ_{zx} ($= \sigma_{zx}$), where the first subscript indicates the direction of the stress; the second subscript indicates the plane normal to the direction in which the stress acts.

In the absence of shear stresses (i.e. when an inviscid fluid is in motion or in case of any type of fluid at rest), the pressure p in a point below the water surface is isotropic, according to the law of Pascal:

$$\sigma_{xx} = \sigma_{yy} = \sigma_{zz} = -p \quad [11]$$

The pressure p is isotropic, because it can be shown that [11] is valid for any orientation of the coordinate system (Van Rijn, 1994). The net force in the x -direction applied to the control volume by the pressure is:

$$-\left(\frac{\partial p}{\partial x} dx\right) dy dz \quad [12]$$

where the negative sign arises, because of a positive pressure acting inward (Cebeci and Bradshaw, 1977).

From figure 9, the forces acting on a fluid element with size Δx , Δy , Δz can be determined. Euler applied the momentum balance equation ($\mathbf{F} = m \cdot \mathbf{a} = d/dt(m\mathbf{v})$) to a fluid element in a gravity field. For incompressible inviscid fluid flow, one obtains for the x , y and z -direction, respectively:

$$F_x = -\frac{\partial p}{\partial x} \Delta x \Delta y \Delta z \quad F_y = -\frac{\partial p}{\partial y} \Delta y \Delta x \Delta z \quad F_z = -\frac{\partial p}{\partial z} \Delta z \Delta x \Delta y - \rho g \Delta x \Delta y \Delta z \quad [13a-c]$$

with the mass of the fluid element given by: $m = \rho \Delta x \Delta y \Delta z$.

Together with the accelerations given by [10], the motion of inviscid fluids can be described, yielding:

$$\begin{aligned} \frac{\partial W}{\partial t} + U \frac{\partial W}{\partial x} + V \frac{\partial W}{\partial y} + W \frac{\partial W}{\partial z} &= -\frac{1}{\rho} \frac{\partial P}{\partial z} - g \\ \frac{\partial V}{\partial t} + U \frac{\partial V}{\partial x} + V \frac{\partial V}{\partial y} + W \frac{\partial V}{\partial z} &= -\frac{1}{\rho} \frac{\partial P}{\partial y} \\ \frac{\partial U}{\partial t} + U \frac{\partial U}{\partial x} + V \frac{\partial U}{\partial y} + W \frac{\partial U}{\partial z} &= -\frac{1}{\rho} \frac{\partial P}{\partial x} \end{aligned}$$

or in vector notation:

$$\frac{D\mathbf{v}}{Dt} = -\frac{1}{\rho}\nabla P + \mathbf{g} \quad [14a-d]$$

Although all real fluids are viscous, in many cases the viscous terms are negligible as compared to the pressure and acceleration terms. An important example of inviscid irrotational (ideal) flow is potential flow. Integration of the Euler equations given by [14] for incompressible irrotational steady flow yields the well-known linear Bernoulli equation which relates velocity, pressure and elevation changes in inviscid fluids (Van Rijn, 1994):

$$H_e = \frac{\mathbf{v}^2}{2g} + \frac{P}{\rho g} + z = \text{constant}$$

where H_e is the total head with respect to a horizontal reference plane.

3.1.2.3 Fluid momentum

Analogous to [5], the rate of change of x, y and z-component momentum of the fluid in the control volume can be expressed as, respectively:

$$\frac{\partial}{\partial t}(\rho U dx dy dz), \quad \frac{\partial}{\partial t}(\rho V dx dy dz), \quad \frac{\partial}{\partial t}(\rho W dx dy dz) \quad [15a-c]$$

Further, the net rate of outflow of x-component momentum via the pair of planes perpendicular to the x-, y- and z-direction are given by, respectively (with similar expressions for the y- and z-component momentum):

$$\frac{\partial}{\partial x}(\rho U^2) dx dy dz, \quad \frac{\partial}{\partial y}(\rho UV) dx dy dz, \quad \frac{\partial}{\partial z}(\rho UW) dx dy dz \quad [16a-c]$$

By using [12], [15] and [16], complemented with body forces, a general expression for the conservation of x-, y- and z-component momentum can be found, which applies to unsteady, three-dimensional compressible flows with body forces (f):

$$\begin{aligned} \frac{\partial \rho U}{\partial t} + \frac{\partial \rho U^2}{\partial x} + \frac{\partial \rho UV}{\partial y} + \frac{\partial \rho UW}{\partial z} &= -\frac{\partial P}{\partial x} + \rho f_x \\ \frac{\partial \rho U}{\partial t} + \frac{\partial \rho U^2}{\partial x} + \frac{\partial \rho UV}{\partial y} + \frac{\partial \rho UW}{\partial z} &= -\frac{\partial P}{\partial x} + \rho f_x \\ \frac{\partial \rho W}{\partial t} + \frac{\partial \rho WU}{\partial x} + \frac{\partial \rho WV}{\partial y} + \frac{\partial \rho W^2}{\partial z} &= -\frac{\partial P}{\partial z} + \rho f_z \end{aligned} \quad [17a-c]$$

Alternatively, realizing that the right-hand side of [17a] is explicitly zero, by subtracting

$$U \left(\frac{\partial \rho}{\partial t} + \frac{\partial(\rho U)}{\partial x} + \frac{\partial(\rho V)}{\partial y} + \frac{\partial(\rho W)}{\partial z} \right)$$

(wherein the continuity equation ([6]) can be recognized) from the left-hand side of the x-component momentum equation [17a], this left-hand side can be written as:

$$\frac{\partial \rho U^2}{\partial x} - U \frac{\partial \rho U}{\partial x} + \frac{\partial \rho UV}{\partial y} - U \frac{\partial \rho V}{\partial y} + \frac{\partial \rho UW}{\partial z} - U \frac{\partial \rho W}{\partial z} + \frac{\partial \rho U}{\partial t} - U \frac{\partial \rho}{\partial t} \quad [18a]$$

Using the differentiation rule for a product, e.g., in [18a] the first two terms satisfy:

$$\frac{\partial \rho U^2}{\partial x} - U \frac{\partial \rho U}{\partial x} = \rho U \frac{\partial U}{\partial x}$$

$$, \quad [18a]$$

reads:

$$\rho \left(\frac{\partial U}{\partial t} + U \frac{\partial U}{\partial x} + V \frac{\partial U}{\partial y} + W \frac{\partial U}{\partial z} \right) \quad [18b]$$

Finally, [17a] can be rewritten, using [18b] and by dividing through the density, ρ :

$$\frac{\partial U}{\partial t} + U \frac{\partial U}{\partial x} + V \frac{\partial U}{\partial y} + W \frac{\partial U}{\partial z} = -\frac{1}{\rho} \frac{\partial P}{\partial x} + f_x \quad [19]$$

which was already derived [14], together with its companion equations for the y- and z-direction, but now complemented with body forces.

When any fluid is at rest on a macroscopic scale (figure 10) or the afore-mentioned inviscid fluid in motion, no tangential stress acts on a surface. There is only the normal stress, i.e., the pressure $-p\delta_{ij}$ (where δ_{ij} is the Kronecker delta; 1 for $i = j$ and 0 for $i \neq j$), which is thermodynamic in origin, and is maintained by molecular collisions. Denoting the additional shear stress by τ_{ij} (figure 9; right) which is due to the relative motion on the continuum scale, the stress tensor (which is symmetric as can be shown with Cauchy's theorem; see e.g., Mei, 2001) can be written:

$$\sigma_{ij} = -p\delta_{ij} + \tau_{ij} \quad [20]$$

where τ_{ij} is called the viscous stress, which, according to Newton's postulation, must depend on gradients of the velocity, that is,:

$$\frac{\partial v_i}{\partial x_j}, \quad \frac{\partial^2 v_i}{\partial x_j \partial x_k}, \quad \dots$$

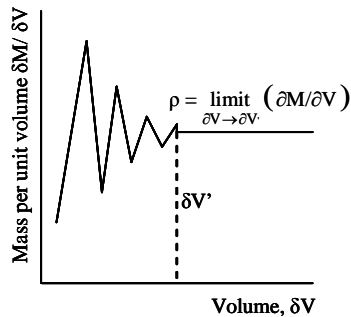


Figure 10. Fluid density. The volume δV of a certain region contains a fluid mass δM . When decreasing δV , the ratio $\delta M / \delta V$ reaches a limiting value, ρ . By further decreasing δV , molecular effects appear and the volume may contain a different total mass of molecules δM at various instants (Van Rijn, 1994). The (extended) continuum hypothesis (I, II) as applied to Navier-Stokes fluids, implies that all macroscopic length and time scales are assumed to be considerably larger than the largest molecular length and time scales (Cramer, 2004).

(I) *Standard continuum hypothesis*: The basis for much of classical mechanics is that the media under consideration is a continuum, meaning that matter is taken to occupy every point of the space of interest, regardless of how closely one examines the material. This continuum hypothesis will break down as the length and time scales of a particular problem become smaller and smaller; at a certain scale, the molecular structure will appear and the standard macroscopic representation can be expected to vanish. Thus, the macroscopic view holds as long as the resultant mathematical model generates results which agree with experiment. Such a model enables one to use the field representation, that is, the view in which the velocities, pressures and temperatures are taken to be piecewise continuous functions of space and time.

(II) *Local thermodynamic equilibrium*: Actually, the Navier-Stokes equations require additional constraints to be valid (Cramer, 2004). Particularly, the constitutive assumptions and the resultant constitutive relations (i.e. the mathematical specification of the material response laws) are only valid when the length and time scales are such that the fluid is in local thermodynamic equilibrium (LTE), i.e., the fluid molecules must adjust their equilibrium state rapidly enough (i.e., within the spatial and temporal gradient scale), or state it differently, the macroscopic process must be sufficiently slow. If the spatial and temporal gradients are too large, the LTE cannot be maintained over the macroscopically imposed time scales and the fluid behaviour is no longer accurately described by the Navier-Stokes equations; one has to return to the kinetic theory and experiment to develop a new model.

It is recognized that for many fluids in nature such as water and air, the relation between the velocity gradient (or rate of strain, or rate of deformation), $\partial v_i / \partial x_i$, and the (shear) stress, τ_{ij} , is linear under most circumstances. Such fluids are known as Newtonian fluids (figure 11).

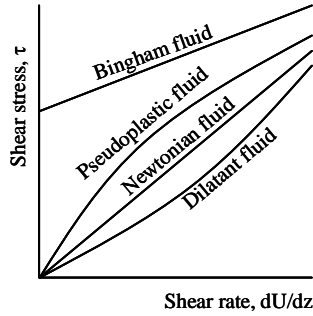


Figure 11. Viscous behaviour of fluids (adapted from Van Rijn, 1994). Fluid systems are characterized by their laminar response to applied shearing stresses. The simplest type of fluid behaviour, that commonly known as Newtonian, is defined by a direct proportionality between shear stress, τ and induced rate of shear, e.g., $\tau = \mu (dU/dz)$, where the constant of proportionality, μ , is called the fluid viscosity. By exclusion, non-Newtonian fluids embrace all fluids that do not conform to this relation; the ratio of shear stress to shear rate becomes an apparent viscosity which varies with the imposed conditions of shear (Dodge, 1959).

Behavioral differences of fluids, solids and visco-elastic materials can be explained by the differences in how they resist deformation, or generally stated, in the way they respond when taken out of equilibrium. The mathematical formulation of these material response laws is referred to as the set of constitutive relations for the considered material, or stress-(rate of) strain relations. For fluids, these are the Navier-Stokes-Fourier conditions that relate the stress tensor ($\boldsymbol{\tau}$), the heat flux vector (\mathbf{q}), the internal energy (e) and the entropy (s) to the field quantities $\rho(\mathbf{r},t)$, $T(\mathbf{r},t)$ and $\mathbf{v}(\mathbf{r},t)$, where ρ is the density, T is the absolute temperature, and \mathbf{r} is the position vector. For Navier-Stokes fluids, the stress tensor, heat flux vector, internal energy and entropy are assumed to depend only on the density ρ , absolute temperature T and the gradients of \mathbf{v} and T . The dependence of the stress on the gradients of the velocity vector can be expressed more simply, by stating that a fluid ought to resist the formation of relative velocity differences. It is this property that distinguishes them from solids, which are assumed to resist relative displacements. A measure of a fluid's resistance to flow is known as its viscosity. The above named constitutive assumptions can be simplified by introducing the requirements that (i) no heat is transferred if the temperature is uniform, regardless of velocity gradients present in the flow and (ii) that no stress can be generated within a Navier-Stokes fluid, solely by temperature gradients. A further restriction to define Navier-Stokes fluids is given by the condition that the afore-mentioned dependencies must be linear in ∇T and $\nabla \mathbf{v}$. This condition of linearity is consistent with the findings of kinetic theory for a fluid that is only slightly out of equilibrium, being the reason for the introduction of LTE in the continuum hypothesis (figure 10). A linear stress-rate of strain relationship is characteristic for a so-called Newtonian fluid.

For second-rank tensors, the most general linear relation is given by (Mei, 2001):

$$\tau_{ij} = C_{ijlm} \frac{\partial v_l}{\partial x_m} \quad [21]$$

where C_{ijlm} is a coefficient tensor of rank 4. In principle, there are $3^4 = 81$ coefficients.

As shown by Spain (1983), in an isotropic fluid the 4th-rank tensor is of the following form:

$$C_{ijlm} = \lambda \delta_{ij} \delta_{lm} + \mu (\delta_{il} \delta_{jm} + \delta_{im} \delta_{jl}) \quad [22]$$

Eighty-one coefficients in C_{ijlm} reduce to two: λ and μ , and [21] reduces to:

$$\tau_{ij} = \mu \left(\frac{\partial v_i}{\partial x_j} + \frac{\partial v_j}{\partial x_i} \right) + \lambda \frac{\partial v_l}{\partial x_l} \delta_{ij} \quad [23]$$

where μ and λ are viscosity coefficients depending empirically on temperature.

It can be seen that the velocity gradient of [23] is made up of two parts, namely, the rate of strain tensor (e_{ij}) and the vorticity ($= \text{curl } \mathbf{v} = \text{twice the angular velocity tensor } \Omega_{ij}$):

$$\frac{\partial v_i}{\partial x_j} = \frac{1}{2} \left(\frac{\partial v_i}{\partial x_j} + \frac{\partial v_j}{\partial x_i} \right) + \frac{1}{2} \left(\frac{\partial v_i}{\partial x_j} - \frac{\partial v_j}{\partial x_i} \right) = e_{ij} + \Omega_{ij} \quad [24]$$

Further, it can be noticed that [23] only depends on the rate of strain, but not on vorticity, which is reasonable, since a fluid in rigid-body rotation should not experience any viscous stress (Mei, 2001). In a rigid-body rotation with angular velocity ω , the fluid velocity is:

$$\mathbf{v} = \boldsymbol{\omega} \times \mathbf{r} \quad v_i = \begin{vmatrix} \mathbf{i} & \mathbf{j} & \mathbf{k} \\ \omega_1 & \omega_2 & \omega_3 \\ x_1 & x_2 & x_3 \end{vmatrix}$$

where the vorticity components are not zero; for example,

$$2\Omega_{12} = \frac{\partial v_1}{\partial x_2} - \frac{\partial v_2}{\partial x_1} = \frac{\partial}{\partial x_2}(\omega_2 x_3 - \omega_3 x_2) - \frac{\partial}{\partial x_1}(\omega_3 x_1 - \omega_1 x_3) = -2\omega_3$$

and hence, τ_{ij} cannot depend on Ω_{ij} , but only on e_{ij} .

The trace of σ_{ij} in [20], i.e., σ_{ii} (pressure excluded) is given by

$$\sigma_{ii} = (2\mu + 3\lambda) \frac{\partial v_i}{\partial x_i} = (3\lambda + 2\mu) \nabla \cdot \mathbf{v} \quad [25]$$

where the bulk viscosity, $k = 3\lambda + 2\mu$ is recognized; μ is the familiar shear viscosity (often denoted as η , the dynamic viscosity, being the product of kinematic viscosity (ν) and density of a fluid (ρ); Van Rijn, 1994) and λ is known as the second viscosity, arising from a fluid's compressibility. The second viscosity is the transport coefficient that dampens the compressional motion of a fluid, beyond the damping caused by the shear viscosity. The damping is the result of energy exchange between the fluid's translational degrees of freedom (acoustic waves or shock waves) and its internal degrees of freedom (molecular rotations, vibrations, metastable intermolecular bonds, and critical fluctuations; Gillis et al., 2005). For most fluids, from experimental experience it is known that the second viscosity can be neglected, explaining the factor -2/3 appearing in [28].

For incompressible fluids, $\nabla \cdot \mathbf{v} = 0$ ([6d]), the viscous stress tensor (cf. [23]),

$$\sigma_{ij} = \mu \left(\frac{\partial v_i}{\partial x_j} + \frac{\partial v_j}{\partial x_i} \right), \quad [26]$$

forming part of the total stress tensor,

$$\sigma_{ij} = -p\delta_{ij} + \mu \left(\frac{\partial v_i}{\partial x_j} + \frac{\partial v_j}{\partial x_i} \right), \quad [27]$$

is known as Stokes' law, simply reading as (Cebeci and Bradshaw, 1977): stress = $2\mu \times$ (rate of strain).

Summarized, like stress is proportional to strain in simple solids (Hooke's law), in simple fluids stress is proportional to rate of strain (Stokes' law). For simple substances, Stokes' law is very accurate; it is valid up to the highest rate of strain ever achieved in practice, even in shock waves, as long as the fluid can be regarded as a continuum (Cebeci and Bradshaw, 1977). Stokes' empirical law gives the surface stresses for fluids, wherein these stresses are just linearly related to the rate of strain, i.e., this law is valid for Newtonian fluids. In case that the fluid can be assumed incompressible,

$$\sigma_{ij} = -p\delta_{ij} + \mu \left(\frac{\partial v_i}{\partial x_j} + \frac{\partial v_j}{\partial x_i} - \frac{2}{3} \delta_{ij} \nabla \cdot \mathbf{v} \right) + (k \delta_{ij} \nabla \cdot \mathbf{v}) \quad [28],$$

reduces to [27].

Thus, for a viscous fluid, the Euler equations [19] can be extended with stress terms denoting the viscous effects, (e.g., for the x-direction reading as:)

$$\frac{\partial \sigma_{xx}}{\partial x} + \frac{\partial \sigma_{xy}}{\partial y} + \frac{\partial \sigma_{xz}}{\partial z} \equiv \frac{\partial}{\partial x} \left[2\mu \frac{\partial U}{\partial x} - \frac{2}{3} \mu \nabla \cdot \mathbf{v} \right] + \frac{\partial}{\partial y} \left[\mu \left(\frac{\partial U}{\partial y} + \frac{\partial V}{\partial x} \right) \right] + \frac{\partial}{\partial z} \left[\mu \left(\frac{\partial U}{\partial z} + \frac{\partial W}{\partial x} \right) \right]$$

i.e., the additional surface stresses (note that $\sigma_{xy} = \tau_{xy}$ and $\sigma_{xz} = \tau_{xz}$), depicted in figure 9 (right), to yield:

$$\begin{aligned}\frac{\partial U}{\partial t} + U \frac{\partial U}{\partial x} + V \frac{\partial U}{\partial y} + W \frac{\partial U}{\partial z} &= -\frac{1}{\rho} \frac{\partial P}{\partial x} + \nu \left(\frac{\partial^2 U}{\partial x^2} + \frac{\partial^2 U}{\partial y^2} + \frac{\partial^2 U}{\partial z^2} \right) \\ \frac{\partial V}{\partial t} + U \frac{\partial V}{\partial x} + V \frac{\partial V}{\partial y} + W \frac{\partial V}{\partial z} &= -\frac{1}{\rho} \frac{\partial P}{\partial y} + \nu \left(\frac{\partial^2 V}{\partial x^2} + \frac{\partial^2 V}{\partial y^2} + \frac{\partial^2 V}{\partial z^2} \right) \\ \frac{\partial W}{\partial t} + U \frac{\partial W}{\partial x} + V \frac{\partial W}{\partial y} + W \frac{\partial W}{\partial z} &= -\frac{1}{\rho} \frac{\partial P}{\partial z} + \nu \left(\frac{\partial^2 W}{\partial x^2} + \frac{\partial^2 W}{\partial y^2} + \frac{\partial^2 W}{\partial z^2} \right) - g\end{aligned}\quad [29a-d]$$

or in vector form (cf. [14d]):

$$\frac{D\mathbf{v}}{Dt} = -\frac{1}{\rho} \nabla P + \nu \nabla^2 \mathbf{v} + \mathbf{g}$$

wherein the fluid is assumed incompressible ($\nabla \cdot \mathbf{v} = 0$); μ ($= \eta = \rho \nu$) and ρ are assumed constant, so that, after rearranging the order of second derivatives, the term $\partial(\nabla \cdot \mathbf{v}) / \partial x$ can be discarded, since it is zero. Body forces are reduced to gravity force only.

Eqs. [29] are often called the Navier-Stokes equations, however, it is emphasized here that, strictly speaking, the term ‘Navier-Stokes equations’, does not refer to the (incompressible form of the) momentum equation only, as can be recognized in many considerations on fluid mechanics (Cramer, 2004). Thus, [29] describe motions for a viscous fluid, under assumption of fluid incompressibility (see Euler equations) and laminar flow conditions (i.e., Newton’s postulation for a highly viscous fluid at low velocities, wherein the fluid flows in parallel layers, so that the shear stress τ at any value of z reads: $\tau = \eta(dU/dz)$; see note of [20]). They are also valid for instantaneous turbulent flow, in the foregoing recognizable by the capitalized notation for the velocities and pressure (U, V, W and P). The given formulations [29] can be extended with additional sources or sinks of momentum, such as e.g. components of the Coriolis forces per unit mass ($(f_x, f_y, f_z)^T = -2\Omega \times (U, V, W)^T$ with Ω being the earth’s rotation vector), external forces by hydraulic structures, discharge or withdrawal of water and wave stresses. Further, they also may be applied under the so-called Boussinesq approximation, stating that if density variations are small, the density may be assumed constant in all terms, except the gravitational term. The Navier-Stokes equations then, for example, read:

$$\begin{aligned}\frac{\partial U}{\partial t} + U \frac{\partial U}{\partial x} + V \frac{\partial U}{\partial y} + W \frac{\partial U}{\partial z} &= -\frac{1}{\rho_0} \frac{\partial P}{\partial x} + \nu \left(\frac{\partial^2 U}{\partial x^2} + \frac{\partial^2 U}{\partial y^2} + \frac{\partial^2 U}{\partial z^2} \right) \\ \frac{\partial V}{\partial t} + U \frac{\partial V}{\partial x} + V \frac{\partial V}{\partial y} + W \frac{\partial V}{\partial z} &= -\frac{1}{\rho_0} \frac{\partial P}{\partial y} + \nu \left(\frac{\partial^2 V}{\partial x^2} + \frac{\partial^2 V}{\partial y^2} + \frac{\partial^2 V}{\partial z^2} \right) \\ \frac{\partial W}{\partial t} + U \frac{\partial W}{\partial x} + V \frac{\partial W}{\partial y} + W \frac{\partial W}{\partial z} &= -\frac{1}{\rho_0} \frac{\partial P}{\partial z} + \nu \left(\frac{\partial^2 W}{\partial x^2} + \frac{\partial^2 W}{\partial y^2} + \frac{\partial^2 W}{\partial z^2} \right) - \frac{\rho}{\rho_0} g\end{aligned}\quad [30a-c]$$

with constant reference density ρ_0 as a mean over the entire fluid volume (Uittenbogaard et al., 1992).

Reynolds found laminar flow only to exist under special hydraulic conditions. Due to eddies created by turbulence, mean flow velocities and pressure show small variations, which are commonly too small to be solved by a numerical model, because of the chosen grid often being too coarse. Solving the exact equations for frequently observed turbulent namely, would require a very fine numerical grid (typically of $O(10^9)$ grid points), because of the turbulent motion containing elements which are much smaller than the extent of the flow domain (typically of $O(10^3)$ smaller; Rodi, 1980). As introduced by Reynolds, a statistical approach is followed, wherein the equations are averaged over a time scale which is long compared to that of the turbulent motion. As a result of this averaging process, unknown terms containing the transport of mean momentum, heat and mass by the turbulent motion arise in the system of equations ([35]), which is, consequently, not closed anymore. A turbulence model is defined as a set of algebraic or differential equations which determines the

turbulent transport terms in the mean-flow equations and thus closes the system of equations. Turbulence models are based on hypotheses about turbulent processes and require empirical input in the form of constants or functions; they do not simulate the details of the turbulent motion but only the effect of turbulence on the mean-flow behaviour.

Reynolds applied the Navier-Stokes equations to turbulent flow by introducing a time-averaging procedure, where each instantaneous variable is represented as a temporal mean value and a fluctuation value:

$$U = u + u', \quad V = v + v', \quad W = w + w', \quad P = p + p' \quad [31]$$

Mean values are defined as follows (e.g. for the velocity in x-direction):

$$\bar{u} = \frac{1}{T} \int_0^T U(t) dt \quad [32]$$

where the period T should be larger than the dominant turbulence scale, but smaller than long periodic effects such as the tidal scale. Substitution of [31] into [30] yields, e.g., for the x-direction:

$$\begin{aligned} \frac{\partial u}{\partial t} + \frac{\partial u'}{\partial t} + \frac{\partial}{\partial x} (u^2 + 2uu' + u'u') + \frac{\partial}{\partial y} (uv + uv' + vu' + u'v') + \frac{\partial}{\partial z} (uw + uw' + wu' + u'w') = \\ - \frac{1}{\rho} \frac{\partial}{\partial x} (p + p') + \nu \left(\frac{\partial^2}{\partial x^2} + \frac{\partial^2}{\partial y^2} + \frac{\partial^2}{\partial z^2} \right) (u + u') \end{aligned} \quad [33]$$

Each term is now averaged over time (T), indicated by an overbar. A similar time-averaging procedure can be executed for the equation of continuity ([6d]): $\partial u / \partial x + \partial v / \partial y + \partial w / \partial z = 0$. Realizing that, by definition, the time-averaged values of the turbulent fluctuation values equal zero, i.e.,

$$\bar{u'} = 0, \quad \bar{uv'} = 0, \quad \bar{vu'} = 0, \quad \bar{uw'} = 0, \quad \bar{wu'} = 0, \quad \bar{p'} = 0, \quad [34]$$

it follows that (under the Boussinesq assumption):

$$\begin{aligned} \frac{\partial u}{\partial t} + \frac{\partial}{\partial x} (u^2 + \overline{u'u'}) + \frac{\partial}{\partial y} (uv + \overline{u'v'}) + \frac{\partial}{\partial z} (uw + \overline{u'w'}) &= -\frac{1}{\rho_0} \frac{\partial p}{\partial x} + \nu \left(\frac{\partial^2 u}{\partial x^2} + \frac{\partial^2 u}{\partial y^2} + \frac{\partial^2 u}{\partial z^2} \right) \\ \frac{\partial v}{\partial t} + \frac{\partial}{\partial x} (vu + \overline{v'u'}) + \frac{\partial}{\partial y} (v^2 + \overline{v'v'}) + \frac{\partial}{\partial z} (vw + \overline{v'w'}) &= -\frac{1}{\rho_0} \frac{\partial p}{\partial y} + \nu \left(\frac{\partial^2 v}{\partial x^2} + \frac{\partial^2 v}{\partial y^2} + \frac{\partial^2 v}{\partial z^2} \right) \quad [35ac] \\ \frac{\partial w}{\partial t} + \frac{\partial}{\partial x} (wu + \overline{w'u'}) + \frac{\partial}{\partial y} (wv + \overline{w'v'}) + \frac{\partial}{\partial z} (w^2 + \overline{w'w'}) &= -\frac{1}{\rho_0} \frac{\partial p}{\partial z} + \nu \left(\frac{\partial^2 w}{\partial x^2} + \frac{\partial^2 w}{\partial y^2} + \frac{\partial^2 w}{\partial z^2} \right) - \frac{\rho}{\rho_0} g \end{aligned}$$

From [35], it can be seen that the velocity fluctuations produce additional terms, which can be interpreted as normal stresses and turbulent shear stresses. The correlations between these fluctuating velocity components (e.g. $\overline{u'u'}$) namely, are responsible for a loss of momentum in the mean flow direction and therefore appear to act as stresses on the fluid. Generally, these so-called Reynolds' stresses are much larger than viscous stresses; for that reason the latter are often neglected (see note of [37]). Eqs. [35] can be rearranged, yielding the Reynolds equations for a fluid element in a turbulent flow:

$$\begin{aligned} \frac{\partial u}{\partial t} + \frac{\partial uu}{\partial x} + \frac{\partial uv}{\partial y} + \frac{\partial uw}{\partial z} &= -\frac{1}{\rho_0} \frac{\partial p}{\partial x} + \frac{1}{\rho_0} \left(\frac{\partial \sigma_{xx}}{\partial x} + \frac{\partial \tau_{xy}}{\partial y} + \frac{\partial \tau_{xz}}{\partial z} \right) \\ \frac{\partial v}{\partial t} + \frac{\partial vu}{\partial x} + \frac{\partial vv}{\partial y} + \frac{\partial vw}{\partial z} &= -\frac{1}{\rho_0} \frac{\partial p}{\partial y} + \frac{1}{\rho_0} \left(\frac{\partial \tau_{yx}}{\partial x} + \frac{\partial \sigma_{yy}}{\partial y} + \frac{\partial \tau_{yz}}{\partial z} \right) \quad [36a-c] \end{aligned}$$

wherein (cf. [26]):

$$\begin{aligned} \sigma_{xx} &= 2\rho \nu \frac{\partial u}{\partial x} + \rho \overline{u'u'} \\ \sigma_{yy} &= 2\rho \nu \frac{\partial v}{\partial y} + \rho \overline{v'v'} \\ \sigma_{zz} &= 2\rho \nu \frac{\partial w}{\partial z} + \rho \overline{w'w'} \\ \tau_{xy} &= \rho \nu \left(\frac{\partial u}{\partial y} + \frac{\partial v}{\partial x} \right) + \rho \overline{u'v'} \\ \tau_{xz} &= \rho \nu \left(\frac{\partial u}{\partial z} + \frac{\partial w}{\partial x} \right) + \rho \overline{u'w'} \\ \tau_{yz} &= \rho \nu \left(\frac{\partial v}{\partial z} + \frac{\partial w}{\partial y} \right) + \rho \overline{v'w'} \end{aligned}$$

[37]

Assuming that $u' \cong w' \cong 0.1\bar{u}$ the turbulent shear stress is approximately $\tau_T = -0.01 \rho \bar{u}^2$ and the viscous stresses are of the order $\tau_v = -\rho \nu \bar{u}/h$. From this, it follows that $\tau_T/\tau_v \geq 100$ for $\bar{u}h/\nu \geq 10000$ meaning that in nearly all cases of interest, the turbulent stresses are much larger than the viscous stresses (Van Rijn, 1994).

How to relate the turbulent stresses (Reynolds stresses) to the u , v and w components is still unknown. This so-called turbulence closure problem is usually solved by introducing the concept of a turbulent viscosity (ε) in analogy with the kinematic viscosity (ν). Application of this eddy viscosity concept, also known as the Boussinesq hypothesis, is based on the idea that Reynolds stresses, like viscous stresses, depend on the deformation of the mean flow. The turbulent shear stress can be represented by (Van Rijn, 1994):

$$\tau_{ij} = -\rho \overline{u'_i u'_j} = \rho \varepsilon \left(\frac{\partial u_i}{\partial x_j} + \frac{\partial u_j}{\partial x_i} \right) \quad [38]$$

$$\text{e.g. } \tau_{yz} = -\rho \overline{v' w'} = \rho \varepsilon \left(\frac{\partial v}{\partial z} + \frac{\partial w}{\partial y} \right) \quad \text{and, for uniform flow } \tau_{yz} = \rho \varepsilon \frac{dv}{dz} = \rho \ell^2 \left| \frac{dv}{dz} \right| \frac{dv}{dz}$$

where ℓ is a mixing length. Instead of ε , the turbulent (or eddy) viscosity is often denoted as ν_T .

Several eddy viscosity distributions have been proposed of which the parabolic distribution, proposed by the mixing length theory of Prandtl is probably the most well-known and simplest one. The mixing length concept states that a fluid parcel travels over a length ℓ before its momentum is transferred. Prandtl assumed that this mixing length is proportional to the distance to the bottom: $\ell = \kappa z$, where κ is known as the constant of Von Kármán (0.4). Substituting this expression for ℓ in [38] results in the familiar logarithmic velocity profile, often being characteristic for alongshore currents in the surf zone (e.g. at Terschelling (Netherlands) during (almost) steady, uniform flow conditions; Houwman (2000) and the (semi-diurnal) tidal currents observed by Gross and Nowell (1983), but only above 1.5m above the bed). Besides algebraic equations (generally suitable for describing steady uniform pressure-driven flow), such as the above-given example, other formulations for the eddy viscosity are available, ranging from relative simple k - ℓ models (also known as one-equation models) to more sophisticated k - ε models (also known as two-equation models). In k - ℓ models, the mixing length is still determined from an algebraic relationship, but the turbulent kinetic energy (tke or k) produced by the roller is described by a differential equation. This k -equation contains terms describing the time dependent effects of production- (resulting from vertical velocity gradients), transport- and dissipation of turbulent kinetic energy (transfer to heat) in the water column. Although good results have been achieved with k - ℓ models in relative simple (including unsteady) flow situations (e.g. Rodi, 1984), however, there is no consensus about a general expression for the mixing length. This illustrates the need for the more complex, but also more generally applicable k - ε model, which is successfully applied in many flow situations (including wave breaking effects; e.g., Van Rijn, 1983; Rodi, 1984; Uittenbogaard&Van Kester, 1996). Herein, a second differential equation is used to describe the dissipation of turbulent kinetic energy, so that the choice for an appropriate mixing length (ℓ) vanishes, since the dissipation rate (ε) is computed from the local flow conditions. This is particular important in unsteady flow. In steady flow, the turbulent kinetic energy is generated in the region near the boundaries. From there, it penetrates in the flow by its own action (turbulent mixing), supporting the local mixing length to be described by a simple, overall mixing length formulation relating the mixing length to the distance to the boundary and the boundary conditions (as given by Prandtl; see e.g. equation 3.22 of Houwman (2000)). Contrarily, in unsteady flow, the local turbulent kinetic energy inside the flow is no longer related to the turbulence level at the boundary at the same time. Consequently, there is no relationship between the local mixing length and the distance to the boundary, in unsteady flow. In that case, the local mixing length or,

alternatively, the dissipation rate ε depends on the local state of turbulence, implying that a k - ε model is requested.

Besides the Boussinesq approximation and hypothesis, one additional assumption, generally known as the shallow-water assumption, is needed to simplify the equations of motion (e.g., [36]), that is, to arrive at the shallow-water equations. Herein, it is assumed that the characteristic horizontal length scale is much larger than the characteristic vertical scale, as is the horizontal velocity compared to the vertical velocity. It is this assumption that supports the decomposition of the turbulent viscosity into a horizontal (ν_T^H) and vertical (ν_T^V) turbulent viscosity. Moreover, since vertical accelerations are assumed to be small compared to the gravitational acceleration in shallow water, the vertical (z) momentum equation, [36c], reduces to the hydrostatic pressure relation (figure 12):

$$\frac{\partial p}{\partial z} = -\rho g \quad \left(\frac{1}{\rho_0} \frac{\partial p}{\partial z} = -\frac{\rho}{\rho_0} g \right) \quad [39]$$

Thus, buoyancy effects or sudden variations in bottom topography, which give rise to vertical accelerations, are not taken into account by this assumption. Taking the origin $z = 0$ at the bottom, integrating [39] results in:

$$p(x, y, z, t) = g \int_z^{\zeta} \rho \, dz + p_a \quad [40]$$

where $\zeta = \zeta(x, y, t)$ is the free surface level relative to the reference plane $z = 0$ and p_a is the atmospheric pressure. Notice that the minus sign present in [39] vanishes here, because of the chosen reference level ($z = 0$ at the bed).

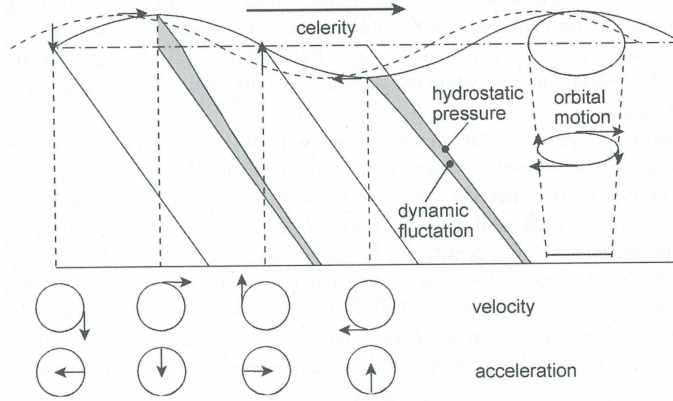


Figure 12. Fluid pressure field under a progressive short wave (adapted from Schiereck, 2004).

Substituting [40] into the pressure term in the momentum equation for the x -direction ([36a]) and using Leibniz' integration rule, yields:

$$-\frac{1}{\rho_0} \frac{\partial p}{\partial x} = -\frac{\rho g}{\rho_0} \frac{\partial \zeta}{\partial x} - \frac{g}{\rho_0} \int_z^{\zeta} \frac{\partial \rho}{\partial x} \, dz' - \frac{1}{\rho_0} \frac{\partial p_a}{\partial x} \quad [41]$$

From [41], it follows that the horizontal pressure gradient is made up of (i) differences of the water level ζ (barotropic term), (ii) density differences in horizontal direction (baroclinic term) and (iii) atmospheric pressure. If the density is assumed to be constant, [40] reads: $p = \rho g(\zeta - z) + p_a$ and the pressure term of [36a]:

$$-\frac{1}{\rho} \frac{\partial p}{\partial x} = -g \frac{\partial \zeta}{\partial x} - \frac{1}{\rho} \frac{\partial p_a}{\partial x} \quad [42]$$

Usually, the atmospheric pressure gradient is neglected; the horizontal pressure gradient is than purely a function of the horizontal water level differences. For example, if the atmospheric pressure gradient is neglected, the density is taken constant, viscous stresses are assumed to be negligible small relative to the turbulent stresses and the shallow water assumption is applied, the momentum equations in x and y -direction may read as (see eqs. [35], [38], [42]):

$$\begin{aligned} \frac{\partial u}{\partial t} + u \frac{\partial u}{\partial x} + v \frac{\partial u}{\partial y} + w \frac{\partial u}{\partial z} &= 2 \frac{\partial}{\partial x} \left(v_T^H \frac{\partial u}{\partial x} \right) + \frac{\partial}{\partial y} \left(v_T^H \left(\frac{\partial u}{\partial y} + \frac{\partial v}{\partial x} \right) \right) + \frac{\partial}{\partial z} \left(v_T^V \frac{\partial u}{\partial z} \right) - g \frac{\partial \zeta}{\partial x} \\ \frac{\partial v}{\partial t} + u \frac{\partial v}{\partial x} + v \frac{\partial v}{\partial y} + w \frac{\partial v}{\partial z} &= \frac{\partial}{\partial x} \left(v_T^H \left(\frac{\partial u}{\partial y} + \frac{\partial v}{\partial x} \right) \right) + 2 \frac{\partial}{\partial y} \left(v_T^H \frac{\partial v}{\partial y} \right) + \frac{\partial}{\partial z} \left(v_T^V \frac{\partial v}{\partial z} \right) - g \frac{\partial \zeta}{\partial y} \end{aligned} \quad [43a-b]$$

where it can be noticed that the $\partial w / \partial x$ term is neglected due to the shallow water assumption.

4 DELFT3D-MODEL FORMULATIONS

4.1 SHALLOW WATER EQUATIONS

Delft3D is an integrated flow and transport modelling system; it consists of several modules of which the flow module (Delft3D-FLOW) forms the hydrodynamic basis. For the present study, there is no need for a coupling with the short-waves model (Delft3D-WAVE), since Snell's law is implemented in the wave and roller energy equations (which are solved in the flow module), allowing a model to be run in profile mode (Van Rijn et al., 2004). For an elaborate overview of the entire numerical modelling system Delft3D, the reader is referred to the various Delft3D User Manuals (WL|Delft Hydraulics, 2005), and, for some test cases, e.g., Lesser et al., (2004).

The flow module solves the afore-explored unsteady shallow-water equations in two (e.g., depth-averaged) or three dimensions. Here, a 2-DV model (alongshore uniformity) is developed. The (incompressible) continuity equation, the horizontal momentum equations, the mass transport equation and a turbulence closure model make up a closed system of equations. It is assumed that modelled flow phenomena have horizontal length and time scales significantly larger than the vertical scales. Since vertical accelerations are assumed small, relative to the gravitational acceleration, these are neglected, so that the vertical momentum equation reduces to the hydrostatic pressure relation (eq. [39]). To fit (land-) boundaries, use can be made of an orthogonal curvilinear coordinate system in which the equations are formulated. For the present study, its simplified form, i.e., a rectangular grid (Cartesian frame of reference) suffices (figure 13).

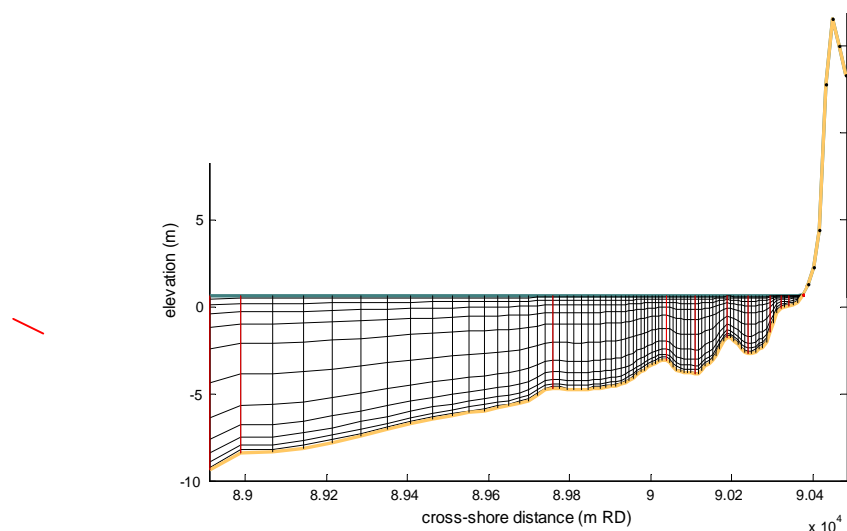


Figure 13. Offshore bed topography (studied cross-shore profile at Noordwijk indicated with a red line) and hydrodynamic model grid draped over seabed (15-10-1979). An intertidal bar, which was present in this transect, has been effaced to force model stability. Further, no attempts were made to test the sensitivity of horizontal and vertical distribution of layers of the computational grid. Instead, the vertical layer distribution (12 layers) is taken from Brière and Walstra (2006); see their table 4-1. Increasing the number of layers in vertical direction (at the water surface and bed, particularly) enables a proper reproduction of momentum transfer due to turbulence. Moreover, the vertical distribution of layers greatly influences bar behaviour, as shown by Brière and Walstra (2006); their figure 4-5. It is assessed that depth-averaged cross-shore and alongshore velocities, as well as the morphology are not very sensitive to a changing horizontal grid resolution; even when the number of grid cells doubles, predicted morphological developments do not vary strongly (Brière and Walstra, 2006; compare results for 70 and 140 cells in their figures 4-7, 4-8 and 4-9). Here, 87 grid cells are chosen in cross-shore direction, with higher resolution in the bar system and on the intertidal beach (smallest cell length of about 9m), where largest variable changes (velocities, sediment transport and bed levels) and spatial variations may be expected. Vertical profiles for which higher temporal (O(hour)) resolution timeseries of computed hydrodynamic and morphodynamic variables are requested, are indicated with red lines; the blue line corresponds to the fluctuating mean waterlevel, which, together with the bed level height (orange line), define the grid cell distribution in the vertical direction at each cross-shore point.

In the vertical direction, a so-called σ -grid (Philips, 1957) is applied, in order to cope with an uneven bed topography. This means that the vertical grid direction is stretched, obeying:

$$\sigma = \frac{z - \zeta}{h} \quad [44]$$

where z is the vertical coordinate, ζ the free surface elevation above the reference plane (at $z = 0$; still water level) and h the total water depth = d (depth below reference plane) + ζ (by definition ≥ 0). Consequently, $\sigma = -1$ at the bottom and $\sigma = 0$ at the free surface. In a σ -coordinate system, the number of layers is the same at every location in the horizontal plane, i.e., the layer interfaces are chosen following planes of constant σ . For each layer, a set of coupled conservation equations is solved.

The partial derivatives in the original Cartesian coordinate system are expressed in σ -coordinates by the chain rule, thereby introducing additional terms (Stelling and Van Kester, 1994). In case of simulations where waves are included (4.4), the hydrodynamic equations are written and solved in a Generalized Lagrangian Mean (GLM) reference frame (Andrews and McIntyre, 1978). In GLM formulation, the wave-induced driving forces averaged over the wave period in the flow equations are more accurately expressed. It extends the standard Eulerian representation with the Stokes' drift components (Walstra et al., 2000). Hereafter, u and v denote the GLM velocity components. The momentum equations in x - (cross-shore) and y (alongshore)-direction in σ -coordinates e.g., read, respectively (noting that $\partial/\partial z = 1/h \partial/\partial \sigma$), see e.g., Lesser et al., 2004; Van Rijn et al., 2004:

$$\begin{aligned} \frac{\partial u}{\partial t} + u \frac{\partial u}{\partial x} + v \frac{\partial u}{\partial y} + \frac{\omega}{h} \frac{\partial u}{\partial \sigma} &= -\frac{1}{\rho_0} p_x + F_x + \frac{1}{h^2} \frac{\partial}{\partial \sigma} \left(v_v \frac{\partial u}{\partial \sigma} \right) + M_x + f_v \\ \frac{\partial v}{\partial t} + u \frac{\partial v}{\partial x} + v \frac{\partial v}{\partial y} + \frac{\omega}{h} \frac{\partial v}{\partial \sigma} &= -\frac{1}{\rho_0} p_y + F_y + \frac{1}{h^2} \frac{\partial}{\partial \sigma} \left(v_v \frac{\partial v}{\partial \sigma} \right) + M_y + f_u \end{aligned} \quad [45a-b]$$

4.2 Vertical momentum equation

The vertical velocity ω is defined at the iso σ -surfaces and computed from the continuity equation:

$$[46] \quad \frac{\partial \zeta}{\partial t} + \frac{\partial hu}{\partial x} + \frac{\partial hv}{\partial y} + \frac{\partial \omega}{\partial \sigma} = Q$$

in which Q represents the contributions per unit area due to the discharge or withdrawal of water, evaporation and precipitation.

ω is the vertical velocity relative to the moving σ -plane and can be thought of as the velocity associated with up-or downwelling motions. It must be realized that the 'physical' vertical velocity (w) in the Cartesian coordinate system, following from

$$w = \omega + u \left(\sigma \frac{\partial h}{\partial x} + \frac{\partial \zeta}{\partial x} \right) + v \left(\sigma \frac{\partial h}{\partial y} + \frac{\partial \zeta}{\partial y} \right) + \sigma \frac{\partial h}{\partial t} + \frac{\partial \zeta}{\partial t}, \quad [47]$$

is not involved in the model equations; its computation is only required for post-processing purposes. Instead, by the shallow-water assumption, the vertical momentum equation is reduced to the hydrostatic pressure equation:

$$\frac{\partial p}{\partial \sigma} = -\rho gh, \text{ which, after integration reads: } p = p_a + gh \int_{\sigma}^0 \rho(x, y, \sigma', t) d\sigma' \quad [48]$$

In case of a non-uniform density, the local density is related to the temperature (T) and density (s) by an equation of state. In Delft3D-FLOW the empirical relation for sea water, given by Eckart (1958), is used:

$$\rho = \frac{1000a}{b + ca} \quad [49]$$

where $a = 5890 + 38T - 0.375T^2 + 3s$, $b = 1779.5 + 11.25T - 0.0745T^2 - (3.80 + 0.01T)s$ and $c = 0.6980$

Here, a space- and time invariant sea water temperature (10°C) and salinity (31‰ (ppt)) are assumed.

4.2.1 Pressure gradients

By Leibniz' integration rule, the following expressions for the horizontal pressure gradients can be obtained, also known as Boussinesq approximations (constant density in all terms of [45], except the gravitational term; cf. [41]):

$$\begin{aligned} -\frac{1}{\rho_0} p_x &= -g \frac{\partial \zeta}{\partial x} - \frac{1}{\rho_0} \frac{\partial p_a}{\partial x} - g \frac{h}{\rho_0} \int_{\sigma}^0 \left(\frac{\partial \rho}{\partial x} + \frac{\partial \sigma'}{\partial x} \frac{\partial \rho}{\partial \sigma'} \right) d\sigma' \\ -\frac{1}{\rho_0} p_y &= -g \frac{\partial \zeta}{\partial y} - \frac{1}{\rho_0} \frac{\partial p_a}{\partial y} - g \frac{h}{\rho_0} \int_{\sigma}^0 \left(\frac{\partial \rho}{\partial y} + \frac{\partial \sigma'}{\partial y} \frac{\partial \rho}{\partial \sigma'} \right) d\sigma' \end{aligned} \quad [50]$$

where the atmospheric pressure (p_a) is taken into account, being important when simulating storm surges.

Obviously, the last term in [50] vanishes if the density of water is assumed constant. For the present study, the density of the seawater ($\rho = 1023 \text{ kg/m}^3$) and air ($\rho_{\text{air}} = 1.0 \text{ kg/m}^3$) are assumed constant.

4.2.2 4.1.3 Reynolds' stresses

The forces F_x and F_y in [45] represent the unbalance of horizontal Reynolds' stresses. As explained before, these stresses are determined using an eddy viscosity concept, in which a flow-dependent eddy viscosity coefficient and corresponding components of the mean rate-of-deformation tensor are multiplied. For 3D shallow water flow, the stress and diffusion tensor are an-isotropic (contrarily to what's has been discussed before [22]). The horizontal eddy viscosity coefficient (ν_H) (and diffusivity coefficient D_H) is assumed to be made up of three parts representing:

- (i) motions and forcings that are not resolved by the horizontal grid (Reynolds' averaged or eddy-resolving computations), which is commonly known as 'sub-grid scale turbulence'; this '2D turbulence' can be determined with a sub-grid scale model (Horizontal Large Eddy Simulation (HLES) that is generally also needed to damp small-scale noise introduced by the advection terms), where the coefficients (ν_H^{2D} and D_H^{2D}) must be based on the model's grid size;
- (ii) '3D turbulence', computed from a turbulence closure model; incorporated vertical coefficients (ν_V^{3D} and D_V^{3D}) are generally an order of magnitude smaller than the horizontal coefficients (ν_H and D_H);
- (iii) molecular (kinematic; ν_{mol}) or horizontal background viscosity; these horizontal eddy viscosity coefficients (ν_H^{back}) and eddy diffusivity coefficient (D_H^{back}) are user-defined.

In other words: $\nu_H = \nu_H^{2D} + \nu_V + \nu_H^{\text{back}}$. For turbulence closure models responding to shear production only, to account for all other forms of unresolved mixing (e.g., internal waves), it may be convenient to specify a background vertical mixing coefficient, which is added to the momentum equation only (third term on rhs of [45]). The vertical eddy viscosity coefficient is then defined by: $\nu_V = \nu_{\text{mol}} + \max(\nu_V^{\text{back}}, \nu_V^{3D})$.

The σ -coordinate system rotates the Cartesian stress tensor and introduces additional derivatives; in Delft3D-FLOW, the stress tensor is redefined in the σ -coordinate system assuming that the horizontal length scale is much larger than the water depth and that the flow is of boundary layer type. The horizontal gradients are taken along σ -planes. Thus, the forces F_x and F_y are of the form:

$$\begin{aligned} F_x &= \frac{\partial \tau_{xx}}{\partial x} + \frac{\partial \tau_{xy}}{\partial y} \\ F_y &= \frac{\partial \tau_{yx}}{\partial x} + \frac{\partial \tau_{yy}}{\partial y} \end{aligned} \quad [51]$$

For small-scale flow, the shear stresses at the closed boundaries must be taken into account (see eqs. [9.22]-[9.24] of Delft3D-Flow Manual, 2005; used in combination with rough side walls (partial-slip)). For large-scale flow simulated with coarse horizontal grids, i.e., when the shear stresses along the closed boundaries may be neglected (free-slip condition), such as for the present study, the forces F_x and F_y are simplified. The horizontal viscosity terms in Delft3D-FLOW then reduces to the Laplace operator along grid lines (where ν_H is assumed constant):

$$\begin{aligned} F_x &= \nu_H \left(\frac{\partial^2 U}{\partial x^2} + \frac{\partial^2 U}{\partial y^2} \right) \\ F_y &= \nu_H \left(\frac{\partial^2 V}{\partial x^2} + \frac{\partial^2 V}{\partial y^2} \right) \end{aligned} \quad [52]$$

4.2.3 External momentum sources or sinks

In [45], the contributions of external sources or sinks of momentum, such as external forces by hydraulic structures, discharge or withdrawal of water and wave stresses, are represented by M_x and M_y . The effects of surface waves on the flow as modelled in Delft3D-FLOW will be described in Section 4.4.

4.2.4 Coriolis force

The Coriolis or geostrophic force term in [45], originates from the earth's rotation, and, hence depends on the geographic latitude (ϕ) and angular speed of the earth ($\Omega = 7.29 \cdot 10^{-5}$ rad/s): $f = 2\Omega \sin\phi$. The Netherlands are located between 50°45' and 53°33' NB; Noordwijk is at approximately 52° NB.

4.2.5 Transport equation

The flows in rivers, estuaries, deltas and coastal seas often transport dissolved substances, salinity and/or heat. The flow module of Delft3D performs the hydrodynamic computations and calculation of the transport of constituents simultaneously, being the reason for exploring the latter, here. In Delft3D-FLOW, the transport of matter and heat is modelled by an (averaged) advection-diffusion equation in three coordinate directions.

Basically, any constituent, except the turbulent kinetic energy (k) and its rate of dissipation (ϵ) is solved with an advection-diffusion equation written in conservative form (Uittenbogaard et al., 1992):

$$\frac{\partial hc}{\partial t} + \frac{\partial huc}{\partial x} + \frac{\partial hvc}{\partial y} + \frac{\partial \omega c}{\partial \sigma} = h \left(\frac{\partial}{\partial x} \left(D_H \frac{\partial c}{\partial x} \right) + \frac{\partial}{\partial y} \left(D_H \frac{\partial c}{\partial y} \right) \right) + \frac{1}{h} \frac{\partial}{\partial \sigma} \left(D_V \frac{\partial c}{\partial \sigma} \right) + hQ \quad [53]$$

with the term hQ denoting the source and sink terms per unit area due to the discharge or withdrawal of water, eventually complemented with the exchange of heat through the free surface; c stands for the concentration of modelled constituent.

To solve the given transport equation, the horizontal and vertical diffusivity (D_H and D_V) need to be prescribed. As previously mentioned, the horizontal viscosity and diffusivity as incorporated in Delft3D-FLOW, are assumed to be a superposition of molecular viscosity, so-called '2D turbulence' and '3D turbulence' (Uittenbogaard et al., 1992). The kinematic viscosity of water is of $O(10^{-6})$ m²/s. '2D-turbulence', being a measure of the horizontal mixing that is not resolved by the advection on the horizontal computational grid, may be computed by a HLES model (Uittenbogaard, 1998; Van Vossen, 2000; Delft3D-Flow Manual, 2005; B-7) or defined as a constant. Here, the contribution of 2D-turbulence, (which thus, has not been taken into account by the implemented 3D-turbulence models), is not directly incorporated. Instead, it is indirectly incorporated by setting the horizontal background viscosity at 0.1 m²/s (Brière and Walstra, 2006), being somewhere in the range commonly used; see e.g., parameter behavioral studies of Ruessink et al., 2001; Ruessink, 2006. The 3D part, D_{3D} , related to the turbulent eddy viscosity follows from a turbulence closure model (§4.1.7). Similar to the total horizontal viscosity coefficient (ν_H), the total horizontal diffusion coefficient (D_H) can be defined as: $D_H = D_H^{2D} + D_V + D_H^{back}$. It is recognized (Delft3D-Flow Manual, 2005) that it may be convenient for turbulence closure models to specify a background vertical mixing coefficient to account for all other forms of unresolved mixing (D_V^{back}). For example, in strongly stratified flows, the turbulent eddy diffusivity at the interface reduces to zero and the vertical mixing reduces to molecular diffusion, which is not realistic because internal waves may be generated. Thus, $D_V = D_{mol} + \max(D_V^{back}, D_V^{3D})$. For use in the transport equation, by means of the Prandtl-Schmidt number (σ_c), the vertical eddy diffusivity is scaled from the vertical eddy viscosity, according to:

$$D_V = \frac{\nu_V}{\sigma_c} \quad [54]$$

in which

$$\sigma_c = \sigma_{c0} F_\sigma(Ri) \quad [55]$$

where σ_{c0} is purely a function of the substance being transported. $F_\sigma(Ri)$ depends on the type of turbulence model that is used; in case of an algebraic turbulence model, $F_\sigma(Ri)$ is a damping function that depends on the degree of density stratification present via the gradient Richardson number (Ri ; see e.g., equation 9.80 of Delft3D-Flow Manual, 2005). If the k- ϵ turbulence model is used, this damping function equals 1, since the buoyancy term in the k- ϵ model automatically accounts for turbulence damping effects caused by vertical density gradients. In case of the modelled sediment being sand, the vertical eddy diffusivity used for the transport calculations may vary from that based on [54]; see van Rijn et al., 2004 and §4.5.1.

4.2.6 Turbulence closure model

In the flow module of Delft3D, several types of closure models are incorporated to determine v_V and D_V ; all models (algebraic eddy viscosity closure model (AEM), k- ℓ model and k- ϵ model, the constant coefficient excluded) share the afore-mentioned eddy viscosity concept (see e.g., [38]). Further, the vertical eddy viscosity, related to a characteristic length scale and velocity scale, has the following form:

$$v_V = c_\mu' \ell \sqrt{k} \quad [56]$$

wherein c_μ' is a calibration constant (derived from the empirical constant (c_μ) in the k- ϵ model: $c_\mu' = c_\mu^{1/4} = 0.09$; table 3 of Rodi, 1980), ℓ is the mixing length and k is the turbulent kinetic energy.

For the present study, a k- ϵ model is used, in which both the turbulent kinetic energy k and the dissipation rate ϵ are produced by production terms representing shear stresses at the bed, water surface and within the flow. The ‘concentrations’ of k and ϵ are subsequently calculated by transport equations.

The mixing length L is determined from ϵ and k via (see Lesser et al., 2004):

$$L = c_D \frac{k\sqrt{k}}{\epsilon} \quad [57]$$

where c_D is a calibration constant ($= 0.1925$; Uittenbogaard et al., 1992).

The output of a turbulence closure model is the eddy viscosity at each layer interface; from this the vertical sediment mixing coefficient is computed via available formulations (e.g., modification by the Van Rijn’s ‘beta-factor’; see §4.5.1).

4.3 BOUNDARY CONDITIONS

4.3.1 Offshore and lateral boundary conditions

To obtain a well-posed mathematical problem with a unique solution, a set of initial and boundary conditions for water levels and horizontal velocities must be specified. Generally, one of the main problems is the specification of suitable boundary conditions at the open boundaries; here a combination of processes acting on the model domain leads to a certain water level or velocity distribution to develop in cross-shore direction. This distribution must be matched by the boundary conditions. Thus, in order to avoid boundary disturbances this distribution must be known, beforehand. Roelvink and Walstra (2004) suggested the model itself to determine the correct solution at the boundary, by imposing the alongshore water level gradient instead of a fixed water level or velocity (see e.g., their figures 2 and 4). Such a boundary condition is known as a Neumann boundary condition. In many cases, the gradient can be assumed zero (Roelvink and Walstra, 2004); it is only for storm surges travelling along the coast or in tidal cases that the alongshore gradient of the water level changes with time. Further, in a model with limited cross-shore extent, the alongshore gradient can be assumed to change hardly in cross-shore direction. For the present study (Noordwijk), at the lateral boundaries (northern and southern limit), these Neumann boundaries are used as gradient type of boundaries for water level. At the seaward (offshore) boundary, an external forcing by the water

level is imposed with a reflection parameter ($\alpha = 200$), to make the open boundary less reflective for short wave disturbances that propagate towards the boundary from inside the model. At these open boundaries, the flow is forced by the tides (astronomic forcing type), implying that the flow conditions are specified using tidal constituents, nodal amplitude and phases as well as a reference date (for determining the nodal amplitude and phase factors). To allow compression of the model input to reduce computational time, time series of the offshore water level and time series of the alongshore water level gradient for the lateral boundaries were made with the Delft3D-TIDE module. These are based on 94 astronomical components of water level and water level gradient interpolated from tidal stations in the vicinity of Noordwijk and centered around beach pole 8000, for the studied period (astronomical boundary conditions; Walstra, pers. comm.). To check the 10-minute predictions, these were converted back to astronomical components. To infer the accuracy of predictions, figure 14 depicts a piece of the entire water level series at the offshore boundary.

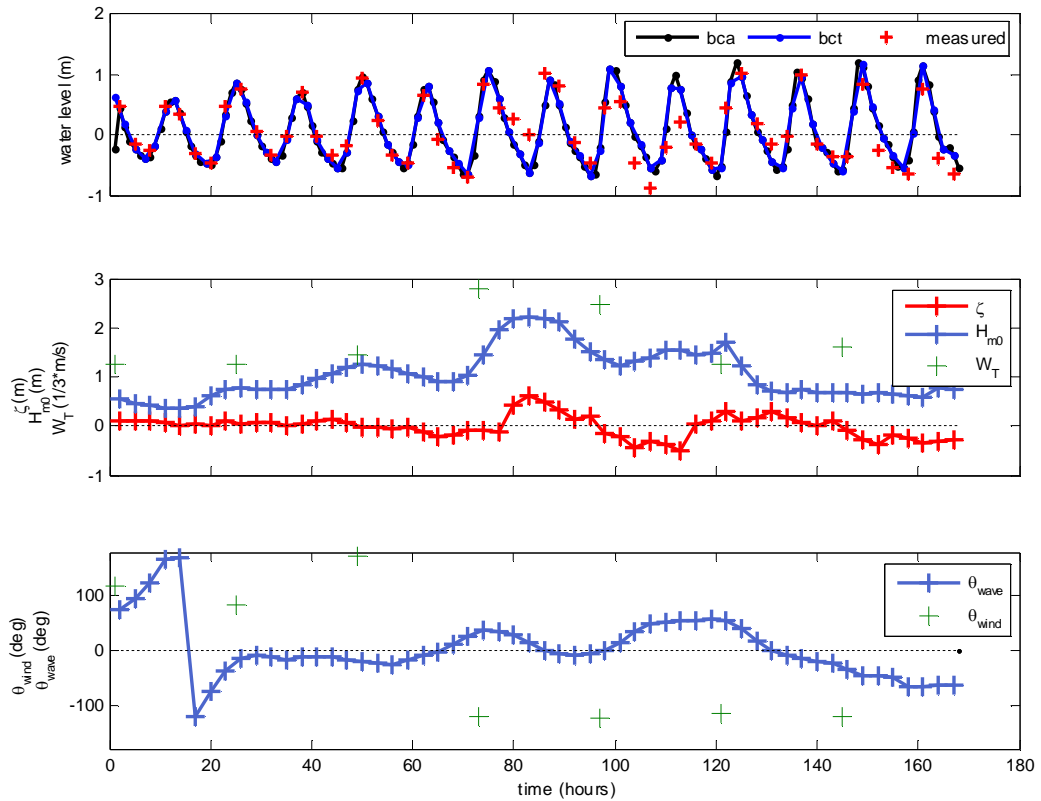


Figure 14. Upper panel: Water level time series at offshore model boundary, (i) based on 94 astronomical components, (ii) constructed time series and (iii) measured ones (per 3 hours). Mid panel: measured set-up/down (interpolated), wave height (spectral) at offshore model boundary and ($1/3^*$) wind speed along vector (daily values at Rotterdam). Lower panel: measured wind- and wave direction in degrees relative to the coast normal, at Noordwijk approximately 28° -inclined to the North.

From figure 14, it can be seen that offshore water level predictions (timeseries) compare well with modelled ones, based on the astronomical components. Deviations from measured water levels are likely due to the prevailing wind and wave conditions (causing set-up/down), as can be inferred from the lower panels. However, measured water levels are provided per 3 hours, which is a rather crude representation of the fluctuating water level. Thus, the reconstructed timeseries of water level and its gradients at the lateral boundaries (eventually in compressed form) are likely to be used in model computations. It is noticed that slightly different settings for northern and southern lateral boundaries led the model to become unstable; therefore, it is decided here to use the same water level gradients for both lateral boundaries. Contrarily to the inflow boundaries (where a uniform velocity profile is prescribed), along closed boundaries (water line) the velocity component perpendicular to the closed boundary is set to zero (a free-slip condition; zero tangential stress).

For the transport boundary conditions, it is assumed that the horizontal transport of dissolved substances is dominated by advection (Lesser et al., 2004), meaning that at the open inflow

boundaries, a boundary condition is needed. For the present study (one sand sediment fraction), a local equilibrium sediment concentration profile is used.

The wave- and wind boundary conditions, (after filtering) imposed at the boundaries are presented in figure 15.

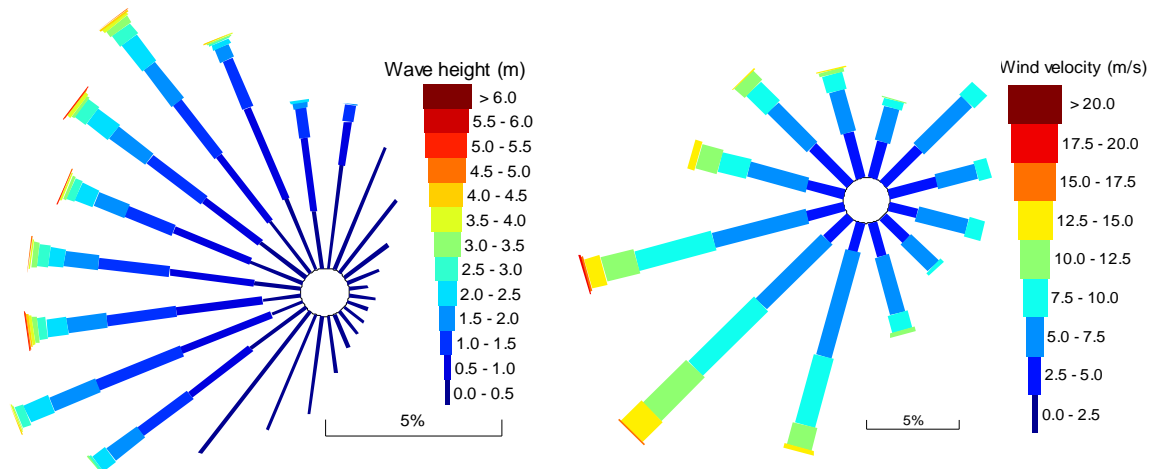


Figure 15. Left: (unfiltered) offshore wave field representation (period: 15-10-1979 upto 05-07-1983) at measurement station 'Meetpost Noordwijk' (MPN; coordinates: RDx = 80.443m, RDy = 476.683m; geographical latitude: NB = 52°16'26" and longitude: OL = 04°17'46", waterdepth \approx 18m). Right: wind field (at 10m height) for the same period, obtained from measurements at wind station 'Rotterdam Geulhaven' (coordinates: RDx = 81.025m, RDy = 434.250m). Measured wind velocities are corrected for the period-mean difference between the wind stations at Noordwijk and Rotterdam (1990-2000; $\Delta W_T = 1.717 \pm 0.0587$ m/s); winds are observed to be somewhat stronger at Noordwijk (likely due to a difference in roughness length: at MPN (open water); 0.002m and at Rotterdam (open land): 0.03m (Royal Netherlands Meteorological Institute)). For a conversion of the roughness length to the more commonly used drag coefficient (C_d), the reader is referred to e.g., §6.2.2 of Houwman, (2000); see also [60b].

It can be noticed (figure 15) that waves coming in from directions larger than 70 degrees relative to the coast normal (orientation of 298°N), are quite common (approximately 30% of the entire considered period, i.e., the studied bar cycle of 3.7 years). From figure 16, it follows that waves from these directions are generally characterized by a lower height and a lower period, with mean heights and periods being somewhat higher for waves from the 2nd quadrant (south-easterly directions) than those coming in from the 1st quadrant (table 1).

For the present study, the wave field is restricted to waves coming in under an angle between 0 and 70 degrees, relative to the coast normal. This restriction is necessary for Snell's law to be used and to avoid possible errors, related to the entrance of offshore propagating waves within the model domain. Further, these conditions cannot be left out of consideration, since this study utilizes a hindcast (no application of a morphological wave climate or morphological wind climate, such as employed by e.g., Van Duin et al., 2004; Walstra et al., 2004; Brière and Walstra, 2006) to investigate cyclic bar behaviour. It may be expected that the contribution of such high-angle incident waves to (total) cross-shore sediment transport is subordinate to (total) alongshore sediment transport.

Table 1. Wave characteristics.

'quadrant' number	angle (°N)	Hm0 (m)	Tm02 (s)	Percentage of occurrence (of total time; 10873 (3-hour) points, (15-10-1979 upto 05-07-1983)) %
		mean \pm std	mean \pm std	
1	8-118	0.61 \pm 0.32	3.66 \pm 0.72	12.63
2	118-228	0.87 \pm 0.52	3.99 \pm 0.73	17.02
3&4	228-(36)8	1.19 \pm 0.78	4.56 \pm 0.81	70.35

Since waves and wind are often correlated (wave- and current-driven transport are often directed similarly), tide-induced transport (particularly affecting alongshore-directed sediment transport, in a cyclic manner) is often of minor influence and net (\sim yearly) bar behaviour is recognized to be a dominant cross-shore oriented process (e.g., among others, Van Enkevort, 2001), intervention by means of replacing these waves by the condition: $Th_0 = 0^\circ$, $H_{m0} = 0.1\text{m}$ and $T_{m02} = 1\text{s}$, probably may be justified. For such a condition, one may expect negligible sediment transport to occur in cross-shore direction. Furthermore, effects of storm(y) conditions may dominate bar behaviour (typically represented by low-angle incident waves), which, indeed, is recognized on the short timescale; offshore migration during storm conditions and onshore bar migration and beach restoration during (enduring) calm-weather conditions (among others, Van Rijn et al., 2003). Alongshore transports are calculated, however, since they are not used for bed level update in the present profile model, by analyzing model predictions, the afore-introduced condition may be verified (i.e., investigating the impact on bar migration).

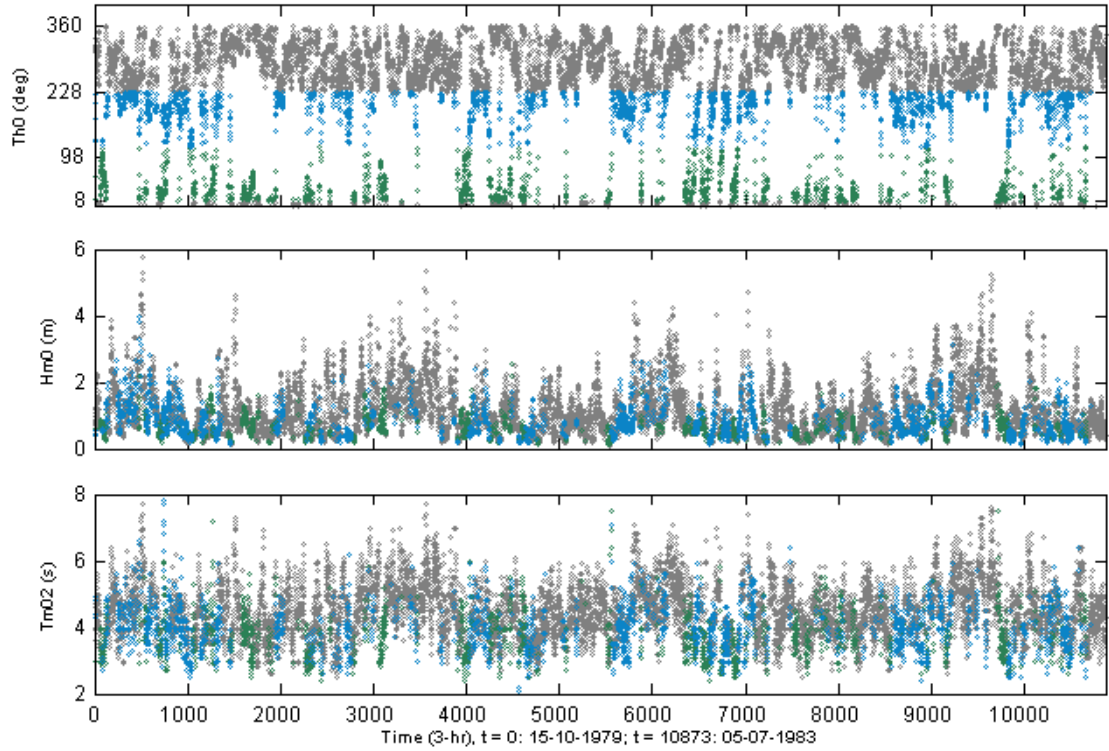


Figure 16. Offshore wave data (0.03-0.5Hz). *Upper panel*: angle of incidence ($^\circ\text{N}$), *mid panel*: wave height (H_{m0} (m)), *lower panel*: wave period (T_{m02} (s)). In each panel, wave angles of 3rd and 4th quadrant (228 -(360) $^\circ$) are represented by gray dots, those of the 1st quadrant (8 - 118°) by green dots and those of the 2nd quadrant (118 - 228°) by blue dots, where the ‘quadrants’ are defined in the coastal coordinate system (see table I).

4.3.2 Vertical boundary conditions

In the σ -coordinate system, the bed and the free surface correspond with σ -planes ($\sigma = -1$ and $\sigma = 0$ respectively). The vertical velocity relative to the moving σ -plane (ω) at these boundaries equals zero, expressing the impermeability of the surface and the bottom. At the seabed, the boundary conditions for the momentum equations read:

$$\left. \frac{v_v}{h} \frac{\partial u}{\partial \sigma} \right|_{\sigma=-1} = \frac{\tau_{bx}}{\rho} \quad \left. \frac{v_v}{h} \frac{\partial v}{\partial \sigma} \right|_{\sigma=-1} = \frac{\tau_{by}}{\rho} \quad [58a-b]$$

where τ_{bx} and τ_{by} are bed shear stress components that include the effects of wave-current interaction. Similarly, the friction due to wind stress at the water surface may be included:

$$\left. \frac{v_v}{h} \frac{\partial u}{\partial \sigma} \right|_{\sigma=0} = \frac{1}{\rho} |\bar{\tau}_s| \cos(\theta) \quad \left. \frac{v_v}{h} \frac{\partial v}{\partial \sigma} \right|_{\sigma=0} = \frac{1}{\rho} |\bar{\tau}_s| \sin(\theta) \quad [59a-b]$$

where θ is the angle between the wind stress vector and the local direction of the grid-line y is constant. The magnitude of the wind shear-stress is defined as:

$$|\vec{\tau}_s| = \rho \bar{u}_s |\bar{u}_s| \quad [60a]$$

Often, the magnitude is determined by the following widely used quadratic expression:

$$|\vec{\tau}_s| = \rho_a C_d U_{10}^2 \quad [60b]$$

where ρ_a is the air density, U_{10} is the wind speed 10 meter above the free surface and C_d is the wind drag coefficient, dependent on U_{10} . Here, a constant $C_d (= 0.002)$ is assumed (see e.g., Houwman, 2000).

For the transport boundary conditions, the vertical diffusive fluxes through the free surface and bed are set to zero.

4.4 SOLUTION PROCEDURE

To solve the partial differential equations, these should be transformed to the discrete space. A thorough treatment of the numerical aspects of Delft3D-FLOW is beyond the scope of the present study. For a full description of the space discretisation, time integration and numerical solution methods applied in Delft3D-FLOW, the reader is referred to the Delft3D-Flow Manual; 2005 and work of Leendertse (1987), Stelling (1984) and Uittenbogaard et al. (1992). The Delft3D-FLOW module is a numerical model based on finite differences. The spatial discretisations of the shallow water equations are performed by draping a grid (here: rectangular) over the model area, whereby the grid is assumed to be orthogonal and well-structured. The variables are arranged in a pattern called the Arakawa C-grid (staggered grid; Lesser et al., 2004; Delft3D-Flow Manual, 2005). In this arrangement, the water level points (pressure points) are defined in the centre of a cell; the velocity components are perpendicular to the grid cell faces where they are situated (see e.g., figure 2 of Lesser et al., 2004; figure 10-3 of Delft3D-Flow Manual, 2005).

4.4.1 Hydrodynamics

To solve the continuity and horizontal momentum equations, Leendertse (1967, 1971, 1973) introduced an alternating direction implicit (ADI) method, wherein one time step is split up into two stages of equal duration. In both stages, all terms of the model equations are solved consistently, with at least second order accuracy in space. For the spatial discretisation of the horizontal advection terms, in the present study the so-called Cyclic method (scheme) of Stelling and Leendertse (1991) is followed. For the water level gradient and the advection terms, time levels are alternating; if in one stage a term is taken implicitly in time, this term will be taken explicitly in time in the other stage. For the entire time step, each separate term is still integrated second-order accurate in time. The advantage of the ADI method is that the implicitly integrated water levels and velocities are coupled along grid lines, leading to systems of equations with a small bandwidth (Lesser et al., 2004). Substitution of the discrete momentum equations in the continuity equation leads to a tridiagonal system of equations for the water levels (Delft3D-Flow Manual, 2005). The computed water levels are substituted back in the discrete momentum equations, so that the velocities can be solved. As stressed by Stelling (1984), a robust solver for the shallow water equations has to satisfy some demands. Besides (i) its suitability for both time-dependent and steady state problems, a solver has to be (ii) unconditionally stable, (iii) accurate (at least second-order) and (iv) computationally efficient. The choice for a certain time integration method (the ADI method being the standard in Delft3D-FLOW), and (subsequent) advection scheme (here: cyclic algorithm) gives rise to a time step limitation, for a model to behave stable and to yield accurate predictions (i.e., avoidance of inaccurately predicted flow patterns; ADI effect; e.g., bad flow field reproduction for regions, characterized by steep bottom gradients). Dependent on the kind of application (e.g., length scale, velocity scale, eventual incorporation of density effects), several time step limitations are available for the shallow water code Delft3D-FLOW (Delft3D-Flow Manual, 2005; Table 10-1). More generally, the Courant number, defined by:

$$Cr = \frac{\Delta t \sqrt{gh}}{\{\Delta x, \Delta y\}} \quad [61]$$

wherein: Δt = time step (seconds), g is gravitational acceleration, h = water depth, $\{\Delta x, \Delta y\}$ is a characteristic value of the grid spacing in either direction (of which the minimum is commonly taken).

gives an indication of the maximum time step that can be used. For critical situations (e.g., flow along irregular (staircase) closed boundaries, flow around islands, flow over tidal flats) the ADI-method is inaccurate for Courant numbers larger than $4\sqrt{2}$. A rough estimate for common situations for which the ADI-method is stable, yielding accurate predictions, is given by the criterion: $Cr < 10$ (Lesser et al., 2004). Based on [61], one can determine a maximum time step to be approximately 12 seconds (0.2 minute) for the present study. This value is determined by taking the maximum $\sqrt{h}/\Delta x$ (computed for each grid cell) value (here: 0.25) where h fluctuates owing to tides, waves, wind and bed level changes. From test simulations, it became clear that a time step of 0.25 minute led the model become unstable. Therefore, for the final model simulations, a time step of 0.1 minute is used. No further sensitivity tests were carried out, however, Brière and Walstra (2006) found stable solutions to be obtained with a time step of 0.2 minute, for their simulations. Consequently, model computational time could have been reduced here with a factor 2. Given the relative long computational time (here, about 13 days were needed to calculate (with a morphological acceleration factor of 2) the considered bar return period of approximately 4 years), it is worthwhile to test several time steps in future modelling activities.

4.4.2 Transport equation

The transport equation, formulated in a conservative form (finite volume approximation) is also solved using the afore-mentioned cyclic method (Stelling and Leendertse, 1991). An algorithm in Delft3D-FLOW accounts for the possible horizontal diffusion along z -planes in the σ -coordinate system, which causes artificial vertical diffusion (Stelling and Van Kester, 1994). This effect arises in areas characterized by steep bed slopes, in combination with vertical stratification. Additionally, a horizontal Forester filter based on diffusion along σ -planes is applied to remove any possible negative concentration values (Lesser et al., 2004). This filter is mass conserving and does not induce significant amplitude losses in sharply peaked solutions (Lesser et al., 2004).

4.5 WAVES

Several processes arise due to wave action in coastal areas (Delft3D-Flow Manual, 2005):

- Enhancement of vertical mixing of momentum due to (i) the generation of turbulence near the water surface by whitecapping and wave breaking, and (ii) energy dissipation near the bottom;
- Generation of a net mass flux, affecting the current profile;
- Generation of cross-shore water level variations (set-up/down) and longshore currents due to variations in the wave-induced momentum flux (radiation stresses). Circulation cells may be generated when the morphology is alongshore inhomogeneous;
- Enhancement of the bed shear stress, affecting the stirring up of sediments and increasing the bed friction.

It is of importance to note that these processes are usually accounted for in a wave averaged manner. Basically, some processes act at a specific location or interface, such as the enhanced bed shear stress or wave breaking at the surface, while others have a certain vertical distribution, such as the energy dissipation due to bed friction in the wave boundary layer. In the σ -coordinate system, Delft3D-FLOW solves the so-called long wave equation, because of the pressure assumed to be hydrostatic (figure 12), which is not obeyed by short waves. The model is not capable of resolving the scales of short waves. For that reason, in analogy with turbulence, the equations of motion are averaged over the wave period (or many wave periods), to obtain the wave-induced force (M_i in [45]). Generally, this wave-induced force can be written as the gradient of the radiation stress tensor ($M_i = -\partial S_{ij} / \partial x_j$),

where wave propagation models are typically used to express S_{ij} in terms of wave parameters (energy, E ; phase and group velocity, c and c_g ; length, L and period T). It must be realized that the afore-mentioned procedure is only justified when the mean motion is uniform with depth. However, this requirement is often not fulfilled for by nature. Consequently, the afore-mentioned GLM method, which writes the flow equations in a coordinate system that moves with the Stokes drift is needed, so that a distinction can be made between the mean and oscillating motion. The computational procedure in the GLM formulation only differs from that applied in the Eulerian formulation at the boundaries. The velocity at the bottom is not the total velocity, but the Eulerian velocity; the bed shear stress is corrected for the Stokes drift. At lateral boundaries, the prescribed velocity is the Eulerian one, while addition of the Stokes drift is performed by Delft3D-FLOW (Delft3D Flow Manual, 2005). In Delft3D-FLOW, the radiation stress gradient is modelled as a shear stress at the water surface. The simplified expression of Dingemans et al. (1987), leaving out all contributions that are not related to dissipation of wave energy, is implemented (see Delft3D-Flow Manual, 2005; p. 9-58):

$$\vec{M} = \frac{D}{\omega} \vec{k} \quad [62]$$

where \vec{M} is the wave forcing due to radiation stress gradients (N/m^2), D is dissipation of breaker energy (W/m^2), ω represents the angular wave frequency (rad/s) and \vec{k} is the wave number vector (rad/m).

An in-depth exploration of the incorporation of other wave-induced processes to Delft3D-FLOW is not given in the present report; the reader is referred to e.g., Delft3D-Flow Manual (2005; Section 9.7 on wave-current interaction), Walstra et al. (2000) and Van Rijn et al. (2004). Here, a brief overview of the effects of wave is given, only:

- The enhancement of vertical mixing of momentum due to shear at the bed is accounted for by the TR2004 parameterisation (see eq. 2.2.15 of Van Rijn et al., 2004, where the nonlinear wave approximation method of Isobe and Horikawa (1982), modified by Grasmeijer (2002), is followed to include the effects of wave asymmetry on the bed shear stress and transport of sediment). Several other methods can be found in the Delft3D-Flow Manual (2005, §9.7.5).
- The wave-induced mass flux is included and is adjusted for the vertically non-uniform Stokes drift (Walstra et al., 2000; Delft3D-Flow Manual, 2005, §9.7.2).
- The additional production of turbulence due to dissipation in the bottom wave boundary layer and by wave breaking and whitecapping is included as extra production terms in the k - ϵ turbulence closure model (Walstra et al., 2000).
- (Longuet-Higgins) streaming (a wave-induced current in the bottom boundary layer, oriented in the direction of wave propagation) is modelled as a time-averaged shear stress, which results from the horizontal and vertical orbital velocities, being not exactly 90° out of phase. This additional shear stress acts across the thickness of the wave boundary layer (Walstra et al. 2000) having its maximum at the top of the layer and decreasing linearly towards the bottom. As shown by Brière and Walstra (2006), streaming has negligible effects on the barred zone, which is recognized to be mainly controlled by offshore-directed flow induced by wave breaking and wave mass transport. Instead, streaming leads to undesirable erosion of the lower shoreface by onshore transports. For that reason, streaming is excluded in the present model ('fwfac = 0').
- Following Reniers et al (2004), infragravity motions can be included. From their model results, it has become clear that these motions are the underlying mechanism for the development of an alongshore quasi-periodic bathymetry of shoals cut by rip channels. As pointed out by Van Rijn et al. (2003), the modelling of low-frequency wave mechanics does not seem to be very important for the simulation of the inner and outer bar behaviour on the storm scale, since the models neglecting low-frequency effects performed reasonably well. Contrarily, low-frequency effects may be of crucial importance for the beach zone.

4.6 SEDIMENT TRANSPORT FORMULATIONS

In most models the convection-diffusion equation, given in eq. [53], forms the basis for computing the transport of suspended sediment. This transport mode is often found to have the major influence

on bar behaviour (among others, Brière and Walstra, 2006; Ruessink, 1998). If the mixing or eddy viscosity coefficient can be taken constant in space and time, analytical solutions can be found, following, e.g., Nielsen (1979) (Van Rijn, 1993). Often, these assumptions can not be carried through, consequently, a numerical solution must be found, which requires the specification of the fall velocity (w_s), the sediment mixing coefficient (ϵ_s) and boundary conditions at the bed and sea surface boundaries (Section 4.2). For an extensive overview of many transport formulations (for both cohesive and non-cohesive sediment) and incorporated processes (e.g., hindered settling, turbulence damping), for both suspended and bed load, in case of currents and waves, or combined, the reader is referred to Van Rijn (1993). For more recent developments, see e.g., Van Rijn and Walstra (2003); Van Rijn et al. (2004); Van Rijn (2006a and 2006b). Several validation tests and sensitivity analyses have been carried out by Brière and Walstra (2006) to investigate the influence of the various parameter(s) (formulation(s)) involved, mainly in terms of bar dynamics (profile model with a morphological tide and morphological wave climate; Walstra et al., 2004). For the present work, the updated TRANSPOR2004 formulations (Van Rijn et al., 2004), implemented in Delft3D, are adopted. These formulations can be combined with the so-called bed roughness predictor (Van Rijn et al., 2004, §2.2.1; Van Rijn, 2006a). Below, a brief overview is given, in order to get some 'top-down feeling' for the formulations.

4.6.1 TRANSPOR2004 - Delft3D

Generally, the bed load transport vector is made up of (i) the current-related transport vector ($q_{b,c}$ (current direction)) and (ii) the wave-related transport vector ($q_{b,w}$ (wave direction)), the latter having a direction which can strongly be affected by the current field (Van Rijn, 1994). The suspended load transport consists of a current-related part due to advective processes ($q_{s,c}$ (current direction)) and a wave-related part, mainly resulting from wave asymmetry effects ($q_{s,w}$ (wave direction, always onshore)). The transition between suspended- and bed load transport is typically assumed to occur at a certain height above the bed (e.g., the well-known reference height 'a' of Van Rijn, 1993). Here, it must be realized that in the updated expressions of TRANSPOR2004, the wave-related suspended sediment transport is also considered as belonging to bed load transport, since it responds almost instantaneously to changing flow conditions (Van Rijn et al., 2004, their §3.2.3; Brière and Walstra, 2006; Delft3D-Flow Manual, 2005, Chapter 11).

4.6.1.1 Bed-load transport of non-cohesive sediment (sand)

Bed load transport is calculated following the afore-mentioned approach of Van Rijn (1993), where it represents the near-bed transport occurring below the reference height, a (Van Rijn et al., 2004; Brière and Walstra, 2006):

$$a = \max(0.5k_{s,c,r}, 0.5k_{s,w,r}, 0.01) \quad \text{and} \quad a = a + \frac{k_{s,c}}{30} \quad \text{if} \quad a < \frac{k_{s,c}}{30} \quad [63]$$

where $k_{s,c}$ is the overall current-related bed roughness, $k_{s,c,r}$ the current-related bed roughness height due to ripples and $k_{s,w,r}$ the wave-related bed roughness height due to ripples. Van Rijn (1993) showed that mega-ripples and dunes are related to the water depth and the flow regime (mobility parameter). The physical bed form roughness of these elements is roughly of the order of half the bed form height. A direct parameterization of this effective (equivalent) bed roughness is proposed by Van Rijn (2006a); thus, herein the effective bed roughness is expressed as a function of the water depth and mobility parameter. Alternatively, bed roughness and shear stress parameters can be based on the well-known Chézy or Manning formulations (see Brière and Walstra (2006; their Section 4.4) for a comparison between these bed roughness formulations, in terms of their effects on predicted bed profiles).

The present approach computes the bed load transport vectors at the water level points and relocates them at the velocity points, using an upwind computational scheme to ensure numerical stability (Lesser et al., 2004; Delft3D-Flow Manual, 2005). It is of importance to notice that the transport equation for bed load is based on the concept of an instantaneous bed shear stress, wherein nonlinear wave effects are taken into account. Further, the bed load vector is modified to account for the slope

of the bed (Brière and Walstra, 2006). The bed load transport components in (m,n)-direction then read, respectively (Brière and Walstra, 2006):

$$q_{b,m} = f_{bed} \frac{u_{b,m}}{|u_b|} q_{b,c} + (f_{bedw} q_{b,w} + f_{susw} q_{s,w}) \cos \phi$$

$$q_{b,n} = f_{bed} \frac{u_{b,n}}{|u_b|} q_{b,c} + (f_{bedw} q_{b,w} + f_{susw} q_{s,w}) \sin \phi$$

[64a-b]

in which: f_{bed} , f_{bedw} and f_{susw} are calibration factors, enabling one to tune the overall significance of each transport component.

As shown by Brière and Walstra (2006), morphologic developments of a bar system (Egmond, the Netherlands, after one year) are strongly determined by the applied scaling of the wave-related bed- and suspended load transports (f_{bedw} and f_{susw}). In the surf zone, the wave-related bed load transport is onshore-directed. Consequently, reducing f_{bedw} (< 0.5) leads to farther offshore migration of the bar system and the profile to become quite irregular (Brière and Walstra, 2006; their figure 4-17). Contrarily, increasing f_{bedw} too much (> 1.5), led the profile to become unrealistic flat, resulting from bed slope effects. Therefore, it is recommended to apply factors in the range of 0.5 to 1.5. In the present study, the wave-related bed load transport is unscaled ($f_{bedw} = 1$). The wave-related suspended load scale factor, f_{susw} , is a function of the complicated γ -phase-factor ($[-1 \ 1]$) proposed by Dohmen-Janssen (1999). The latter factor is incorporated to account for the wave-related suspended transport to be eventually directed against the direction of wave propagation, depending on the bed form roughness and the magnitude of the asymmetric wave motion. Brière and Walstra (2006) showed that an increase of f_{susw} results in a reduction of the offshore bar migration, whereas lower values suppress morphological developments, by smoothing the bed profile (their figure 4-19). This is due to the fact that wave-related suspended load transports are added to the bed load, which is affected by bed slope gradients. Therefore, they suggest a f_{susw} -value of 0.3, which is adopted here. Current-related transports are offshore oriented as a result of wave breaking and Stokes drift. Scaling of the current-related transport (f_{bed}) is observed to hardly influence bar dynamics on a time scale of 1 year (Brière and Walstra, 2006; their figure 4-16). $u_{b,m}$, $u_{b,n}$ and $|u_b|$ are the Eulerian velocity components and magnitude in the bottom computational layer, ϕ is the local angle between the direction of wave propagation and the computational grid ($^\circ$). For more details on the computation of the bed load transport, in case of the presence of waves, and including the wave-related suspended sediment transport (with a phase lag coefficient (γ) of 0.1), one is referred to Van Rijn (2006a), Brière and Walstra (2006) and Van Rijn et al. (2004).

4.6.1.2 Suspended-load transport of non-cohesive sediment (sand)

The current-related suspended load transport, defined as the transport of sediment by the time-averaged current velocities, and including the wave stirring on the sediment load (Brière and Walstra, 2006), follows from:

$$q_{s,c} = f_{sus} \int_{z_a}^h cu \, dz$$

[65]

where f_{sus} is a calibration factor; Brière and Walstra (2006) found a strong correlation between this scaling factor and migration rate of the bar system, implying that this type of sediment transport dominates bar behaviour. Besides, f_{sus} also affects beach morphological processes, significantly (see their figure 4-15). It is observed that large coefficient values (f_{sus} between 0.6 and 2) causes unrealistic erosion of the upper part of the profile. Commonly, f_{sus} is taken to be 1.0 (Brière and Walstra, 2006). Further, h = water depth, z_a is the height of a ([63]), c is the concentration profile and u is the velocity profile, including eventual effects of wave-current interaction.

As follows from [65], the current-related suspended sediment transport is calculated by taking the product of the velocity profile and the concentration profile, which is obtained by solving the advection-diffusion equation ([53]; $c = F(\text{effective fall velocity, bed shear velocity, near-bed Richardson number})$). As mentioned before (§4.1.6 and §4.1.7), the vertical eddy diffusivity given by [54] needs to be modified in case of the modelled sediment being sand. To incorporate the difference

between fluid and granular diffusion (Van Rijn, 1994), the so-called Van Rijn's β -factor is introduced, thereby extending [54] into:

$$D_V = \beta \frac{v_V}{\sigma_c} \quad [66]$$

where the β -factor (limited between 1 and 1.5; Van Rijn et al., 2004) may written as:

$$\beta = 1 + 2 \left(\frac{w_s}{u_{*,c}} \right)^2 \quad [67]$$

where: w_s = sediment fall velocity (depending on the sediment size; see e.g., Van Rijn, 1994; Van Rijn et al., 2004; §3.2.3.2. As shown by Brière and Walstra (2006; their figure 4-25), the grain size has a marked effect on bed profile developments) $u_{*,c}$ is the current-related bed shear stress velocity (see e.g., Brière and Walstra, 2006; Appendix A-3).

Eq. [67] is only valid for situations without waves (Lesser et al., 2004); for simulations including waves, using the k - ε turbulence closure model, [67] needs slight modification. As Van Rijn's β -factor is intended to apply to the current-related mixing only, the β -factor applied to the total mixing computed by the k - ε model can be reduced to an effective β -factor (Lesser et al., 2004):

$$\beta_{\text{eff}} = 1 + (\beta - 1) \left(\frac{\tau_c}{\tau_w + \tau_c} \right) \quad [68]$$

wherein τ_c and τ_w are the current- and wave-related bed shear stresses, respectively; β follows from [67].

In the updated TRANSPOR2004 formulations, the β -factor is expressed differently to [68]; see Brière and Walstra (2006; A-6). In the present study, the vertical diffusion coefficients are computed from the Van Rijn's parabolic-linear mixing distribution for current-related mixing ('epspar = true'). The equilibrium sediment concentration profile is reconstructed following a well-known Rouse law (see e.g., Van Rijn et al., 2004, eq. 3.2.60; Brière and Walstra, 2006, Appendix A-6) and the concentration below the reference level is fixed to the reference concentration (c_a). Moreover, the sediment mixing coefficients can be calculated entirely apart from the turbulence closure model; the wave-related sediment mixing coefficient near the bed can be found using the updated expression of TRANSPOR2004 (Van Rijn, 2006b).

Finally, it should be noticed that sediment transported below the reference height is regarded as belonging to bed load transport; this means that sediment transported below the reference height must be subtracted to the suspended sediment transport, to prevent double counting (correction vector; see Brière and Walstra, 2006; their §2.2.6 and A-7; Van Rijn et al., their figure 3.2).

4.7 MORPHODYNAMICS

The exchange of sediment between the bed and the water column can be modelled using sink and source terms acting on the near-bottom layer that is entirely above Van Rijn's reference height (a). This first computational cell above ' a ' is called the reference layer (or 'kmx layer', for short; Van Rijn et al., 2004). The sediment concentration in the cells that lie below the kmx layer are assumed to rapidly respond to changes in the bed shear stress, and have the same concentration as the reference layer (Van Rijn et al., 2004). Each half time step, source and sink terms model the erosive flux from the reference level due to upward diffusion and the deposition flux due to sediment settling. The quantity of sediment entering the flow due to upward diffusion, and dropping out of the flow due to sediment settling are given by, respectively (Van Rijn et al., 2004):

$$E = D_V \frac{\partial c}{\partial z} \quad [69a]$$

$$D = w_s c_{\text{kmx, bottom}}$$

[70a]

wherein: D_v is the sediment diffusion coefficient evaluated at the bottom of the kmx cell (often denoted as ε_s) and $c_{\text{kmx,bottom}}$ is the concentration at the bottom of the kmx cell ($= \alpha_1 c_{\text{kmx}}$, where α_1 is a correction factor and c_{kmx} is the average concentration of the kmx cell; see Van Rijn et al., 2004; their eq. [3.2.62]). It is noted here that E and D are actually determined per sediment fraction; in the present study, however, only one fraction (sand) has been incorporated. See Van Rijn et al., 2004 and Lesser et al., 2004 for details.

In TRANSPOR2004, [69a] and [70a] are approximated by the following expressions, respectively:

$$E \approx \alpha_2 \varepsilon_s \left(\frac{c_a - c_{\text{kmx}}}{\Delta z} \right) \quad [69b]$$

$$D \approx \alpha_1 c_{\text{kmx}} w_s \quad [70b]$$

where: α_2 is a correction factor for sediment concentration (Van Rijn et al., 2004; their eq. [3.2.63]), Δz is the difference in elevation between the centre of the kmx cell and Van Rijn's reference height ($= z_{\text{kmx}} - a$).

Finally, [69b] and [70b] are subdivided into a source and sink term, which can be solved, subsequently. More details can be found in Van Rijn et al. (2004).

The bed level can then be updated (per half a computational time step), by taking the net sediment change due to (i) suspended transport (difference between source and sink terms) and (ii) bed load transport ([64]), with (iii) the correction for suspended sediment transport below the reference height (a) taken into account. Mathematical formulations are provided by Lesser et al. (2004). Before updating bed levels, the suspended and bed load transports can be multiplied by a so-called morphological acceleration factor, to deal with the difference in time scales between hydrodynamic and morphologic developments. This implies that long morphological simulations can be achieved using hydrodynamic simulations of only a fraction of the required duration (for an example, the reader is referred to e.g., Brière and Walstra, 2006; their table 3-1). For the present study, there is no direct need for such a morphological scale factor (hindcast). However, as suggested by Walstra (pers. comm.), computational time may be reduced tremendously, when use is made of this factor. Accordingly, model input has to be compressed with applied morphological scale factor.

4.8 PARAMETER SETTINGS

For convenience, table 2 lists the main model parameters applied in the present Delft3D profile model.

Table 2. Summary of parameter settings applied in the computations

Parameter	Value/Setting	Description
<i>Grid</i>		
Anglat	52 °	Latitude of model centre (Coriolis)
MNKmax direction	[87 3 12]	Grid dimensions; number of cells in cross-shore, alongshore and vertical
Thick depth (σ -grid)	[2; 3.2; 5; 7.9; 12.4; 19.6; 19.6; 12.4; 7.9; 5; 3.2; 1.8]	Layer thickness from top to bottom in percentage (%) of total water
<i>Constants</i>		
Ag	9.81 m/s ²	Gravitational acceleration
Rhow	1023 kg/m ³	Water density
Rhoa	1.0 kg/m ³	Air density
Tempw	10 °C	Water temperature
Salw	31 ppt	Salinity

Wstres speed))	[0.00063; 0; 0.00723; 100]	Wind drag coefficients ([1 st breakpoint; wind speed; 2 nd breakpoint; wind
Dt	6 s	Computational time step
Dryflc	0.1 m	Minimum depth of drying and flooding
<i>Waves (including rollers and application of Snell's law)</i>		
GamDis (H/h)	-1	Breaker criterion of Ruessink et al. (2003), based on local condition
Betaro but of utmost	0.05	Steepness of wave front (not very important for wave height modelling, importance for current modelling; see e.g., Ruessink et al., 2001), see also B-14 of Delft3D-Flow Manual (2005)
F_lam	0.00	Breaker delay of Roelvink et al., 1995; their eq. (1)
<i>Roughness</i>		
Roumet	Manning	Type of bottom friction formulation
Ccofu	$0.026 \text{ m}^{1/3} \text{ s}^{-1}$	Uniform bed roughness in u-direction
Ccofv	$0.026 \text{ m}^{1/3} \text{ s}^{-1}$	Uniform bed roughness in v-direction
Rouwav formulation	VR04	Bottom stress formulation due to wave action; here TRANSPOR2004
Irov (shear) stresses	free	Wall roughness; type of slip condition (free/partial/no); here tangential at boundaries are neglected (§4.1.3), i.e., a free-slip condition is applied.
<i>Viscosity</i>		
Vicouv	$0.1 \text{ m}^2/\text{s}$	Uniform background horizontal eddy viscosity (§4.1.6)
Dicouv	$0.1 \text{ m}^2/\text{s}$	Uniform background horizontal eddy diffusivity ($\sigma_v = 1$; see §4.1.6)
Htur2d	No	(en/dis)abling use of HLES subgrid model ('2D turbulence'; §4.1.3)
Vicoww	$0.000001 \text{ m}^2/\text{s}$	Uniform background vertical eddy viscosity (§4.1.6)
Dicoww	$0.000001 \text{ m}^2/\text{s}$	Uniform background vertical eddy diffusivity (§4.1.6)
Xlo	0 m	Ozmidov length scale
Tkmod	k-ε model	Type of turbulence closure model ('3D-turbulence')
<i>Sediment</i>		
Namc1	Sediment sand	Type of sediment (sand or mud)
RhoSol	2650 kg/m^3	Sediment density
SedDia	200 μm	Median sediment (sand) diameter (d_{50})
SedD10	150 μm	d_{10}
SedD90	300 μm	d_{90}
CDryB	1600 kg/m^3	Dry bed density
Iopsus conditions and d_{50}	1	Suspended sediment size is calculated dependent hydrodynamic
FacDSS FacDSS*SedDia)	1.0	Factor to determine initial suspended sediment diameter (=
<i>Morphology</i>		
MorFac	2	Morphological scale factor (note that boundary conditions (timeseries of waves/wind/astronomic water level) need to be compressed with this factor, too)
MorStt the	120 minutes	Start time for bed updating (relative to simulation start time); smoothing hydrodynamic boundary conditions
Thresh	0.2 m	Threshold sediment thickness for reducing sediment exchange
MorUpd	yes	Updating bathymetry during flow run
EqmBc	yes	Equilibrium sediment concentration profile at open (inflow) boundaries
DensIn	no	Including the effect of sediment on water density; here, water density is assumed constant; there is no need for an extension of Eckart's empirical relation (eq. [49]) (see Lesser et al., 2004; their eq. 18)
AksFac (where $k_s =$	1.0	Factor to determine Van Rijn's reference height (a) = $AksFac * k_s$ effective bed roughness); (sub-paragraph 4.5.1.1)
RWave ripple height.	1.0	Factor to determine wave related bed roughness = $RWave * \text{estimated}$
AlfaBs	1.0	Longitudinal bed gradient factor for bed load transport (§4.5.1)

AlfaBn	50	Transverse bed gradient factor for bed load transport (§4.5.1)
Sus	1.0	Suspended transport factor (§4.5.1)
Bed	1.0	Bed load transport factor (§4.5.1)
SusW	0.3	Wave-related suspended transport factor (§4.5.1)
BedW	1.0	Wave-related bedload transport factor (§4.5.1)
SedThr	0.1 m	Minimum depth for sediment calculations
ThetSD	1.0	Fraction of erosion to assign to adjacent dry cells
FWFac	0.0	Tuning parameter for wave streaming (Section 4.4)
EpsPar	true	Only for waves in combination with k-ε turbulence model (sub-paragraph 4.5.1.2)
mixing		true : Van Rijn's parabolic-linear mixing distribution for current-related mixing
UpdInf		false: vertical sediment mixing values from k-ε turbulence model true: down-wind approach, false: bed level constant
NeglectEntrainment	true	Concept for morphology updating due to suspended transport

5 MODEL RESULTS

The present chapter aims at presenting some exploratory results (a phenomenological approach) of the afore-described profile model (with settings given in table 2, unless specified otherwise).

5.1 MORPHOLOGICAL ACCELERATION FACTOR

As mentioned, usage of a morphological scale factor to accelerate morphological developments greatly favours computational time. Determination of the model's sensitivity to changing upscaling factors is thus indispensable. Figure 17 depicts predicted cross-shore bed profiles after one year, for different factors.

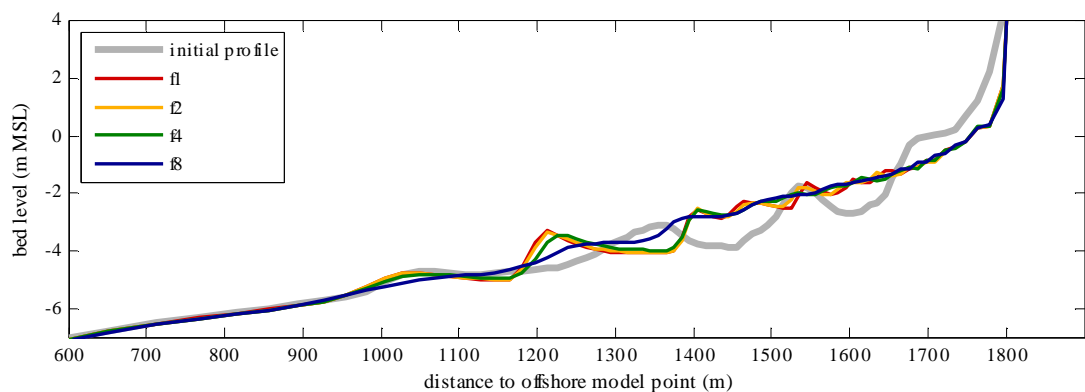


Figure 17. Comparison between 4 predicted (after one year) cross-shore bed profiles for different morphological acceleration factors (hence, compression of time series of boundary conditions (tides, winds, waves) with these factor-values (f1, f2, f4, f8). Default parameter settings were used (table 2, but with time step = 0.25 minute). It should be noted that the correction vector (subparagraph 4.5.1.2) of the suspended sediment transport was wrongly implemented in the algorithm (not reversed in the flow transport solver). However, it is questionable whether this significantly affects total computed sediment transport, since suspended sediment transport generally dominates total sand transport (figure 23). The initial bed profile (measured at 15-10-1979, but without intertidal bar) is given by the gray-coloured line.

As can be seen from figure 17, the outer bar zone gets a flattened appearance for increasing factors of time series compression (factor = 8), which is in contrast with field observations. For all factors, though more pronounced for higher compression factors, the morphologic development of the inner bar zone is badly reproduced. Moreover, and likely being (partly) associated with the former, the intertidal area and dune foot are eroded excessively. For that reason, implementation of a fixed layer is inevitable. Only slight differences are recognized between application of no morphological factor (f1) and a factor of 2 (f2). Therefore, it is decided to carry out longer-term computations with a morphological acceleration factor of 2.

5.2 FIXED LAYER

A fixed layer is implemented in the profile model to prevent the intertidal area and dune foot from being eroded enormously. It is questioned here, at what cross-shore location the seaward limit of the fixed layer should be located. Figure 18 shows model results for different seaward extensions of the implemented layer: at (approximately) mean water line (MWL), low water line (LWL) and at $z = -2.6\text{m}$ NAP ($\approx \text{MSL} \approx \text{MWL}$), respectively. It can easily be recognized that incorporation of a fixed layer yield improved results, in terms of maintenance of the bar system (figure 18). Of interest is the similar behaviour of the outer bar zone ($x < 1450\text{m}$ approximately) for the implemented fixed layers at different heights, perhaps suggesting that farther offshore located bars are less sensitive to shallow water processes (e.g., in view of the outer bar zone to act as a hydrodynamic filter, thus indeed controlling inner bar zone morphologic behaviour). Furthermore, predicted morphologic developments within this zone compare well with results of the model in which no fixed layer is used. Contrarily, the height at which a fixed layer is implemented, greatly influences the morphological behaviour of the inner bar zone. In all cases, a new bar is generated at the foot of the beach face, followed by its offshore migration. Meanwhile, the outer bar migrates offshore and changes shape (seaward oriented face becoming relative steep, whereas the opposite occurs at the landward-facing side), however, it is still far from its final decaying stage. As can be seen from figure 18, the higher the seaward limit of the fixed layer is positioned, the more seaward the newly generated bar is predicted to be migrated after one year. Further, it is assessed that the generation and migration of a new bar coincides with erosion and steepening of the beach face, if the fixed layer does not extend to the inner subtidal trough (cf. green and yellow lines with blue line in figure 18).

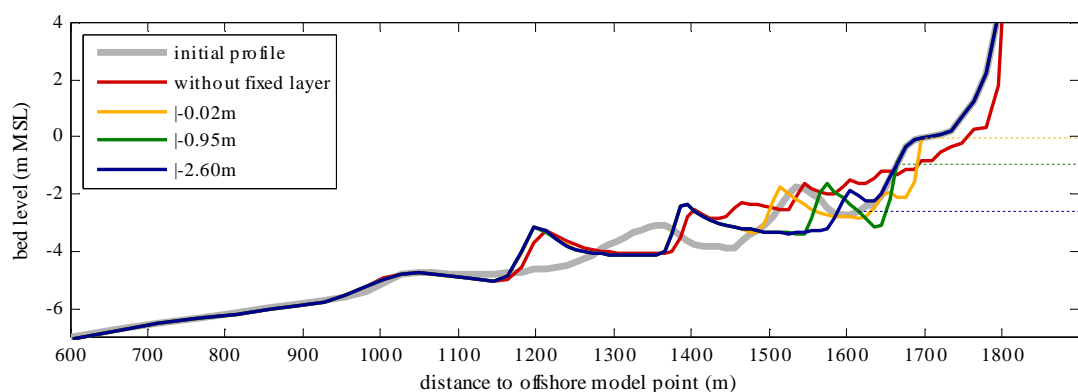


Figure 18. Morphologic developments after one year for different heights of the implemented fixed layer (dashed lines). Default parameter settings were used (table 2). The models in which a fixed layer was implemented were solved with the correct flow transport solver. For comparison, model result without a fixed layer is shown, also.

Obviously, one may wonder what is the effect of different fixed layer heights on the long-term behaviour of the bar system. Figure 19 shows that bars that existed in the initial profile, migrated further offshore and show somewhat decreasing bar amplitudes after 1.5 year. In case of a fixed layer at (approximately) MWL, even a fourth bar is generated, pointing at an overestimation of observed offshore migration of the bar system (cf. Brière and Walstra, 2006).

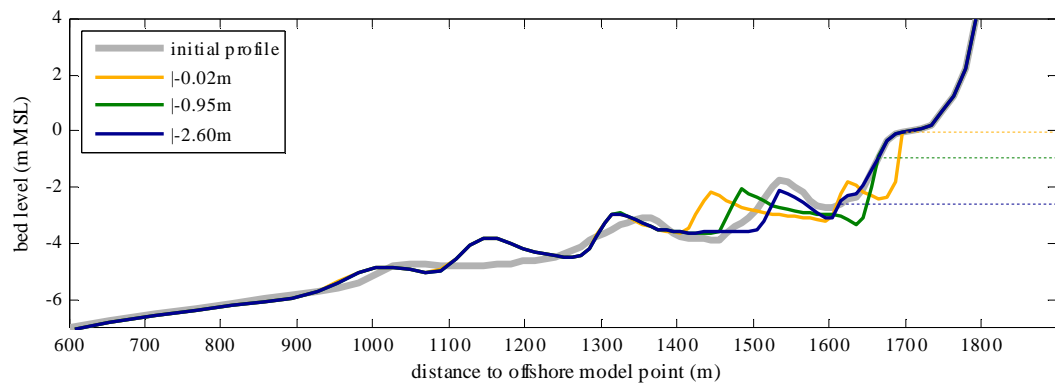


Figure 19. See figure 18, but now computed bed profiles after 1.5 year are shown. Different implemented seaward extensions of a fixed layer clearly controls predictions of a newly formed bar.

Unfortunately, after 1.5 year, in the model with a fixed layer at about MWL, an error in the wave module arised. It is therefore, decided to use a fixed layer extending towards the LWL for longer-term computations.

5.3 TRANSVERSE BED GRADIENT FACTOR

The bed roughness formulation appeared to have the major effect on the modelling of natural bar dynamics (Brière and Walstra, 2006; see also implication at figure 3, text). Herein, bed slope effects may play an important role, as they modify the bed load transport vector (as well as wave-related suspended sediment transport) in the TRANSPOR2004 formulations. The commonly used default value of the transverse bed gradient factor (f_{ALFABN}) amounts 1.5. As can be seen from figure 20, both coefficient values produce morphologic irregularities; the default value of 1.5 clearly leads to a wave train alike barred profile. Contrarily, $f_{ALFABN} = 50$ generally leads to damping of morphologic entities; it is only the outer bar that maintains its bar shape. In both cases, the upper part of the profile suffers from unrealistic erosion again, demonstrating the need for a fixed layer (Section 5.2).

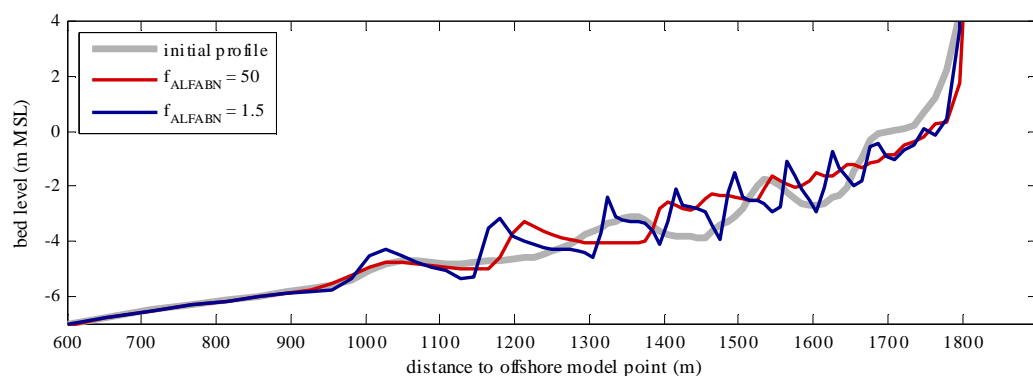


Figure 20. Morphologic developments after one year for two different values of the coefficient (f_{ALFABN}), needed for the computation of the transverse bed slope, which modifies the direction of the bed load transport vector (subparagraph 4.5.1.1). Default parameter settings were used (table 2), but with astronomic tidal boundary conditions (no morphological acceleration factor) and a time step of 0.25 minute. See figure 17 for note on flow transport solver. No fixed layer was implemented.

Moreover, the combination of a default transverse bed slope factor of 1.5 and implementation of a fixed layer does not yield reliable morphologic predictions (figure 21). Here, a high value of 50 seems to better reproduce natural bar dynamics. Obviously, this is only a crude approximation, likely

accounting for other unresolved processes. Therefore, future modelling studies should include a thorough sensitivity analysis on this aspect.

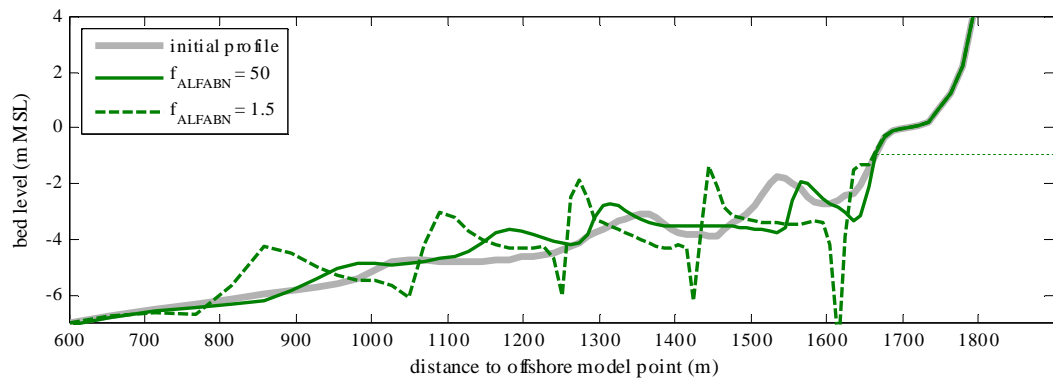


Figure 21. Morphologic developments after one observed bar return interval (about 4 years) for two different values of the coefficient (f_{ALFABN}) are shown. See table 2 for model settings, but with a fixed layer at $z = -0.95\text{m}$.

5.4 ANALYSIS OF PREDICTED LONG-TERM BAR BEHAVIOUR

This section highlights modelled bar behaviour with model settings presented in table 2, complemented with a fixed layer at approximately LWL. In figure 22, measured and modelled cross-shore bed profiles are compared.

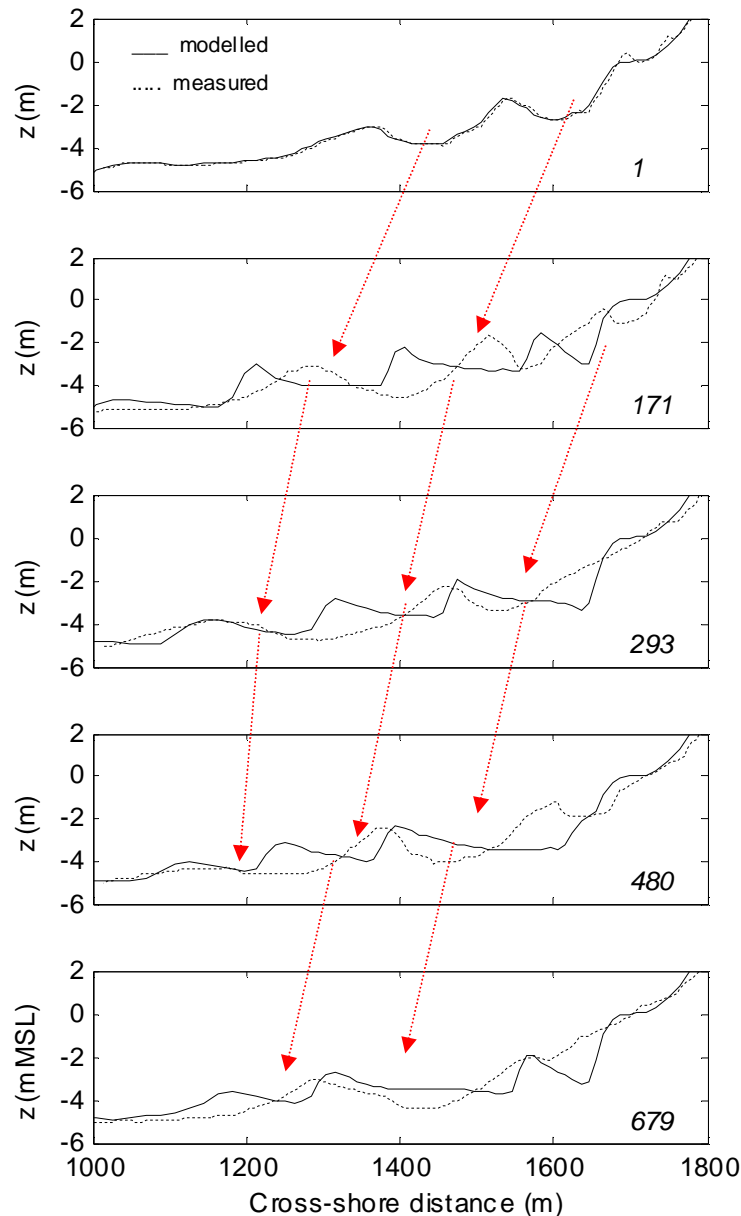


Figure 22. Comparison of measured and modelled bed level heights. Dates (2* days after 15-10-1979; lower right corner of each panel) correspond to: 15-10-1979, 19-09-1980, 22-05-1981, 02-06-1982, 05-07-1983, respectively.

It is unequivocally clear that the present model is not capable of accurately reproducing observed cross-shore bed profiles. Both shape and cross-shore position of bars cannot be predicted, accurately (figure 22). The modelled outer troughs are too flat, as compared to observations, or probably better stated: the landward-oriented slopes of the outer and middle bar are too gentle. Further, generation of a new bar is preceded by unrealistic deepening (steepening) of the trough (beach face), which separates the subtidal area from the intertidal area. Throughout the model run, velocity gradients near MSL are frequently predicted much too large ($> 5\text{ m/s}$ per 0.5 a time step) than one may expect to

occur. Overall speaking, the model is capable of reproducing cyclic bar behaviour (arrows in figure 22). However, as also pointed out by Brière and Walstra (2006), the Delft3D models which have been set up thus far, seem to overestimate the offshore migration of the bar system. Since the wave- and current field can be predicted reasonably well by profile models (Van Rijn et al., 2003), it is likely that sediment transport formulations must be further improved, to obtain more realistic morphologic developments. Brière and Walstra (2006) suggest to mainly attempt to improve the predictions of the wave-related suspended load transport. According to their sensitivity analyses, an increased suspended wave-related onshore transport results in unrealistic flattening of the bed profile, which is caused by bed slope effects that are acting on the combined wave-related bed load and suspended load transports in the present transport formulations. Therefore, they suggest to (i) consider both modes of transport separately and (herewith associated) (ii) to exclude bed-slope effects on the wave-related suspended sediment transport.

To further study modelled cyclic bar behaviour, figure 23 depicts some modelled hydrodynamics, sediment transport and (resulting) morphology, each making up the components of the coastal morphodynamic system.

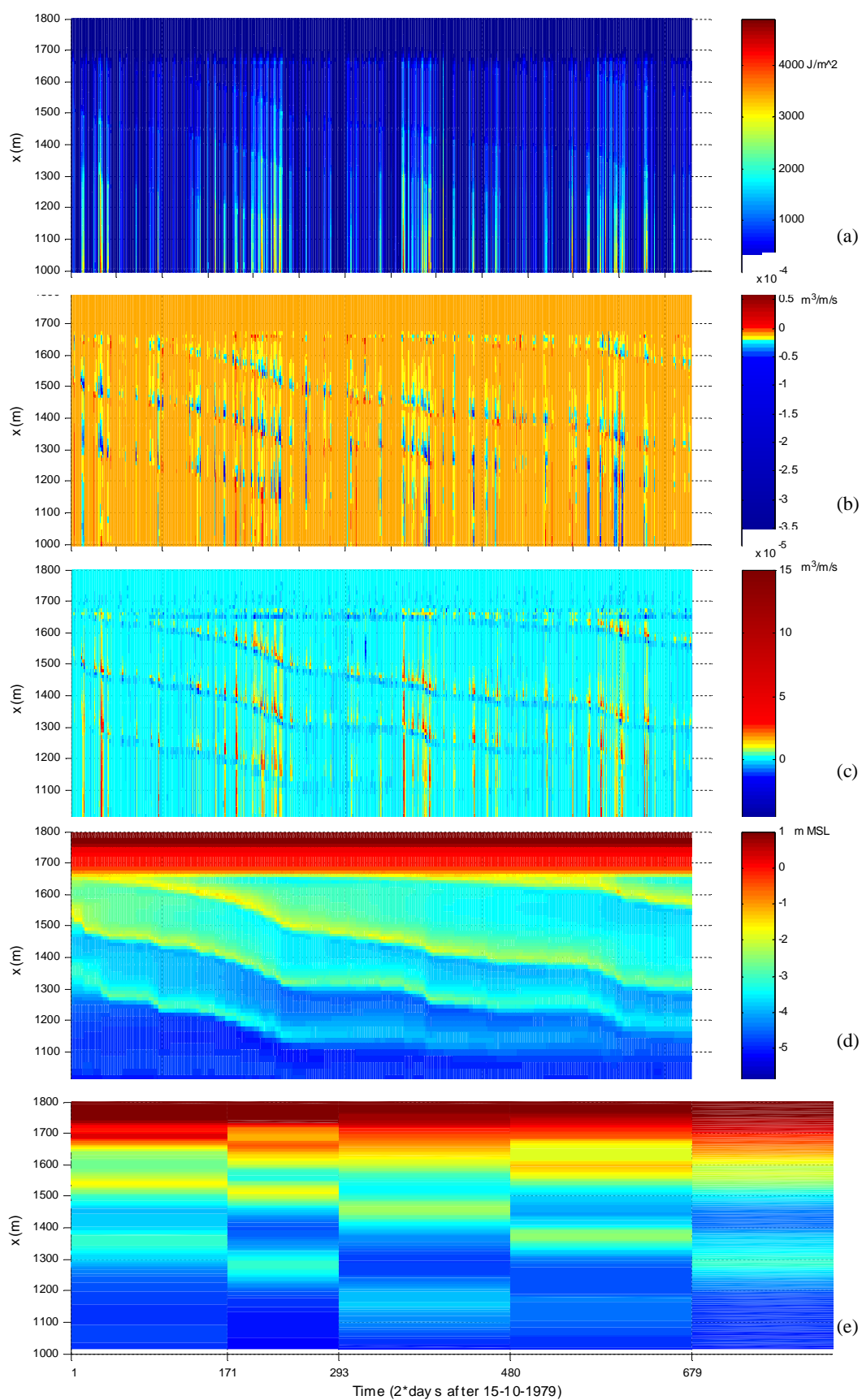


Figure 23. Modelled short-wave energy (a), combined wave- and current-related cross-shore suspended- (b) and bed (c) load transport, and bed level height (d) at 87 cross-shore points, with daily temporal resolution. For comparison, measured bed level heights are given in (e). Alongshore transports (gradients) are not used for bed level update. A fixed layer at $z = -0.95\text{m}$ prevents (modelled) unrealistic erosion of the intertidal beach and dune foot, likely being the result of omitted processes (e.g., infragravity waves) and assumptions which are not fulfilled for (e.g., absence of alongshore morphologic nonuniformities, which could have driven alongshore sediment supply), besides the presence of small longshore transport gradients due to slight numerical inaccuracies, which cannot be avoided (Brière and Walstra, 2006).

By comparing the upper and lower panel of figure 23, one may conclude that ‘spikes’ in short-wave energy (storm periods) accelerate the offshore-directed bar migrational trend. Fair-weather periods are predicted to affect migration of the most inner bar, particularly. More offshore located bars (deeper water) are less vulnerable to this calm weather periods; the bar flattens, however, its crest position remains virtually constant. The predicted ongoing offshore movement of a bar in very shallow water ($h < 3\text{m}$ approximately, such as the most inner bar shown here) is in agreement with the given hypothesis in Ruessink (1998; Section 7.2). Herein, it is postulated that a bar in its initial state does not seem to exhibit a net tendency to move either onshore or offshore, on an annual scale. This implies that the offshore annual transport approximately equals the onshore annual transport. However, if the annual frequency distribution of H/h in the inner bar zone changes, the aforementioned equilibrium is disturbed. A shift towards more wave breaking conditions (or more intense breaking) can be expected to increase the annual offshore transport relative to the annual onshore transport. Such a shift towards more frequent and/or more intense surf zone conditions in the inner bar zone may be established by the increasing water depth over a decaying outer bar (Ruessink, 1998; Ruessink and Terwindt, 2000).

As can be seen from the mid panels of figure 23, the total sediment transport is predicted to be strongly dominated by the suspended load (note the different scales) (cf. Ruessink, 1998; the horizontal velocity asymmetry of short waves and the undertow being the most important small-scale hydrodynamic processes to be incorporated, for upscaling to medium-scale morphodynamics). Maximum values for both transport modes are typically predicted for storm(y) conditions, while during low-energetic conditions, less sediment transport is predicted to occur. Of interest is the predicted cross-shore varying direction of the total bed load transport, especially for storm(y) conditions. Generally, the total suspended sediment transport is directed similarly, across the entire profile. As expected, maximum offshore-directed suspended load transports are found over the bar crests (up to $-3.5 \times 10^{-4} \text{ m}^3/\text{m/s}$), with much lower predicted values for the troughs (-0.03 to $-0.13 \times 10^{-4} \text{ m}^3/\text{m/s}$). Onshore predicted suspended load transports are also computed, for some periods, however, they do not show distinct patterns and are usually not larger than $0.07 \times 10^{-4} \text{ m}^3/\text{m/s}$. Contrarily, opposite directions in bed load transport can be recognized across the profile, for storm(y) periods, particularly (e.g., period [200-250] days). At the bar crests, small offshore-directed bed load transports are predicted (about $-0.16 \times 10^{-4} \text{ m}^3/\text{m/s}$), whereas in the troughs onshore-directed bed load transports are commonly predicted (0.05 to $0.3 \times 10^{-4} \text{ m}^3/\text{m/s}$ with outliers up to $1.5 \times 10^{-4} \text{ m}^3/\text{m/s}$). The transition between onshore and offshore directed bed load transports is found to be quite sharp, likely indicating the effects of the bed slope. Moreover, this transition seems to vanish at the outer bar for increasing outer bar depths (period [350-400] days and period [575-600] days), i.e., for a decaying outer bar (cf. Ruessink and Kroon, 1994).

6 CONCLUSIONS & RECOMMENDATIONS

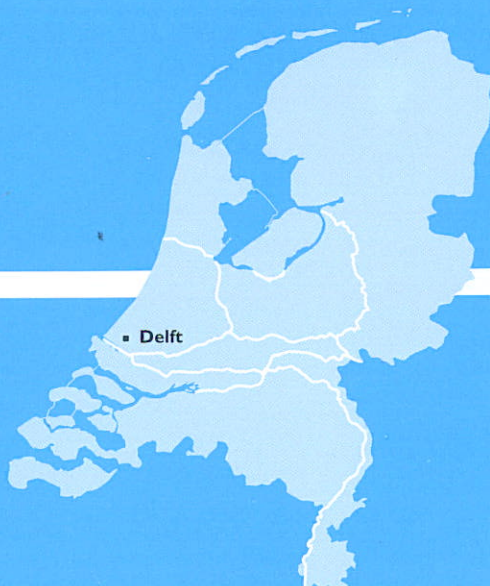
The present study revealed that a profile model, based on the shallow-water equations, complemented with a $k-\varepsilon$ turbulence closure model and the TRANSPOR2004 sediment transport formulations (Van Rijn et al., 2004), is capable of reproducing frequently observed *cyclic* bar behaviour along sandy, uninterrupted coasts, though mainly in a qualitatively manner. A bottom-up modelling approach (hindcast) was employed to model one recurrence interval of about 4 years at the Noordwijk site, which forms part of the Holland coast, being the study object of several earlier studies (e.g., Wijnberg and Terwindt, 1995; van Enckevort, 2001). The main findings of this study are summarized below, complemented with some recommendations for future modelling activities.

- It has become clear that a fixed layer need to be incorporated in the present model, to prevent for unrealistic erosion on the intertidal area and near the dune foot. This area is typically affected by processes having a 3-D character (e.g., Reniers et al., 2004), which are not accounted for in the present study. Further, although constant gradient conditions are adopted in longshore direction, Brière and Walstra (2006) assessed small longshore transport gradients, which can not be avoided. The offshore extension of a fixed layer is observed to be a determinant factor for the location of generation, and subsequent offshore migration of a new bar (figure 19). Contrarily, fixed layers at different heights do not control morphological behaviour of (initially) existing outer bar zone. A thorough analysis of the (long-term) effects of fixed layers on bar behaviour may form the subject of future modelling studies.
- Though the implemented transport formulations have been proven to better describe both hydrodynamics and sediment transport (Van Rijn et al., 2004; Brière and Walstra, 2006), considerable uncertainty related to the bed roughness still exists (likely being reflected by the unrealistic high value of the transverse bed gradient factor used in the present work). Particularly, onshore suspended load transport due to asymmetric oscillatory wave motion forms a source of uncertainty; as suggested by Brière and Walstra (2006), here included bed slope effects on the suspended wave-related transports should be excluded. Improving the former will possibly improve the rate of modelled offshore migration of the bar system, which is overestimated in the present study.
- As pointed out by e.g., Wijnberg (1995) (and also deducible from model predictions; figure 23), observed cyclic bar behaviour is not related to changes in offshore forcing, as the wave climate lacks cyclicity on the same scale as the bar cycle. From presented model predictions (Section 5.4), it followed that the outer bar crest depth indeed seems to control its own degeneration and the offshore migration of landward bars. This points at the importance of morphologic feedback mechanisms in the nearshore system as is hypothesized in earlier studies (e.g., Ruessink and Terwindt, 2000). Free behaviour of a coast's morphology possibly demands for a top-down modelling approach, wherein the system may be modelled in terms of simpler, carefully chosen set of equations derived from empirical study of the system (Thornton et al., 2000; see also Section 2.3). The presence of feedbacks in the system suggests that both the chronology of wave events and initial morphological state are not the key factors for longer-term behaviour of the bar system (e.g., Southgate and Capobianco, 1997). Yet, these feedback mechanisms (which may have both a local (referring to the bar morphology itself) and non-local character (referring to the morphology of seaward located bars)) are not well understood, although considerable progress is on the way (Plant et al., 2001; Ruessink et al., 2003). Thus, future modelling efforts may use morphological wave- and tide climates (e.g., van Duin et al., 2004; Brière and Walstra, 2004) to investigate underlying mechanisms for cyclic bar behaviour. This is even more supported by the relative long computational time needed for the present modelling study, although (i) being successfully reduced by a factor 2 (by means of application of a morphological acceleration factor) and (ii) usage of larger time steps is here not tested thoroughly (§4.3.1).

7 REFERENCES

- ABDELRAHMAN, S.M., E.B. THORNTON, 1987. Changes in the short wave amplitude and wavenumber due to the presence of infragravity waves, *Proceedings Coastal Hydrodynamics*, ACSE, pp. 458-478.
- BRIÈRE, C., D.J.R. WALSTRA, 2006. Modelling of bar dynamics, Report Z4099.00 Delft Hydraulics.
- BURROUGH, P.A., R.A. MCDONNELL, 1998. *Principles of Geographical Information Systems*, Oxford University Press.
- CEBECEI, T., P. BRADSHAW, 1977. *Momentum transfer in boundary layers*, Hemisphere Publishing Corporation, ISBN 0-07-010300-3.
- CRAMER, M.S., 2004. *Notes on Navier-Stokes equations*, Cambridge University Press, www.navier-stokes.net.
- DELFT HYDRAULICS, 2005. *Delft3D-Flow Manual*, WL|Delft Hydraulics.
- DINGEMANS, M.W., A.C. RADDER, H.J. DE VRIEND, 1987. Computation of the driving forces of wave-induced currents, *Coastal Engineering*, 11, pp. 539-563.
- DODGE, D.W., 1959. *Fluid systems*, E.I. du Pont de Nemours & Co., Inc., Buffalo, N.Y. (Vol. 51, No.7).
- GRUNET, N.M., B.G. RUESSINK, D.J.R. WALSTRA, 2005. The influence of tides, wind and waves on the redistribution of nourished sediment at Terschelling, The Netherlands, *Coastal Engineering*, 52, pp. 617-631.
- HOUWMAN, K., 2000. Tide, wind- and wave-driven flow processes in the nearshore zone- Field measurement Terschelling and modelling, PhD. Thesis, Utrecht University, Netherlands, pp. 235
- KROON, A., 1994. Sediment transport and morphodynamics of the beach and nearshore zone near Egmond, The Netherlands. PhD. Thesis, Utrecht Univ., 275 pp.
- LEENDERTSE, J.J., 1987. A three-dimensional alternating direction implicit model with iterative fourth order dissipative non-linear advection terms. WD-333-NETH, The Netherlands Rijkswaterstaat.
- LESSER, G.R., J.A. ROELVINK, J.A.T.H.M. VAN KESTER, G.S. STELLING, 2004. Development and validation of a three-dimensional morphological model, *Coastal Engineering*, 51, pp. 883-915.
- PLANT, N. G., M. H. FREILICH, R. A. HOLMAN, 2001. Role of morphologic feedback in surf zone sandbar response, *Journal of Geophysical Research* 106, 973-989, 2001.
- PLANT, N.G., R.A. HOLMAN, M.H. FREILICH, W.A. BIRKEMEIER, 1999. A simple model for interannual sandbar behaviour, *Journal of Geophysical Research*, 104, pp. 15,755-15,776.
- RENIERS, A.J.H.M., J.A. ROELVINK, E.B. THORNTON, 2004. Morphodynamic modelling of an embayed beach under wave group forcing, *Journal of Geophysical Research*, Vol. 109, C01030.
- RODI, W., 1980. Turbulence models and their application in hydraulics- A state of the art review, Institut fur Hydromechanik, University of Karlsruhe, Presented by the IAHR-Section on Fundamentals of Division II: Experimental and Mathematical Fluid Dynamics.
- ROELVINK, J.A., TH.J.G.P. MEIJER, K. HOUWMAN, R. BAKKER, R. SPANHOFF, 1995. Field validation and application of a coastal profile model, *Coastal Dynamics '95*.
- ROELVINK, J.A., M.J.F. STIVE, 1989. Bar generating cross-shore flow mechanisms on a beach. *Journal of Geophysical Research*, 94, pp. 4785-4800.
- ROELVINK, J.A., D.J.R. WALSTRA, 2004. Keeping it simple by using complex models, The 6th Int. Conf. On Hydrosience and Engineering (ICHE-2004), Brisbane, Australia.
- RUESSINK, B.G., 1998. Infragravity waves in a dissipative multiple bar system. PhD Thesis. Utrecht University, Netherlands, 245 pp.
- RUESSINK, B.G., 2006. A Bayesian estimation of parameter-induced uncertainty in a nearshore alongshore current model.
- RUESSINK, B. G., A. KROON, 1994. The behaviour of a multiple bar system in the nearshore zone of Terschelling: 1965-1993, *Mar. Geol.*, 121, 187-197.
- RUESSINK, B.G., J.R. MILES, F. FEDDERSEN, R.T. GUZA, S. ELGAR, 2001. Modeling the alongshore current on barred beaches, *Journal of Geophysical Research*, 106, C10, 22451-22464.
- RUESSINK, B.G., K.M. WIJNBERG, R.A. HOLMAN, Y. KURIYAMA, I.M.J. VAN ENCKEVORT, 2003. Intersite comparison of interannual nearshore bar behaviour, *Journal of Geophysical Research*, Vol. 108, No. C8, 3249.
- SCHIERECK G.J., 2004. Introduction to bed, bank and shore protection.

- SOUTHGATE, H.N., M. CAPOBIANCO, 1997. The role of chronology in long-term morphodynamics. Theory, practice and evidence. Paper submitted to the Coastal Dynamics '97 proceedings, 10pp. Book of Abstracts, pp. 194-195. In: RUESSINK, B.G., 1998. Infragravity waves in a dissipative multiple bar system. PhD Thesis. Utrecht University, Netherlands, 245 pp.
- STELLING, G.S., 1983. On the construction of computational methods for shallow water flow problems. Ph.D. Thesis, Delft Univ. of Techn., Delft.
- STELLING, G.S. AND KESTER, VAN J.A.T.M., 1994. On the approximation of horizontal gradients in sigma coordinates for bathymetry with steep bottom slopes. *Int. J. Num. Meth. Fluids*, Vol. 18, 915-955.
- THORNTON, E., T. DALRYMPLE, T. DRAKE, S. ELGAR, E. GALLAGHER, B. GUZA, A. HAY, R. HOLMAN, J. KAIHATU, T. LIPPMANN, T. OZKAN-HALLER, 2000. State of Nearshore Processes Research: II, Report based on the Nearshore Research Workshop, St. Petersburg, Florida, Technical Report NPS-OC-00-001, Naval Postgraduate School, Monterey, California.
- UITTENBOGAARD, R.E., 1998. Model for eddy diffusivity and viscosity related to sub-grid velocity and bed topography. Note, Delft Hydraulics.
- UITTENBOGAARD, R.E., J.A.T.H.M. VAN KESTER, G.S. STELLING, 1992. Implementation of three turbulence models in TRISULA for rectangular horizontal grids (including 2DV test cases), Delft Hydraulics.
- UIJTTEWAAL, W., Turbulence in hydraulics, CT5312, Environmental Fluid Mechanics Section, Faculty of Civil Engineering and Geosciences, Delft University of Technology (Lecture notes).
- VAN DUIN, M.J.P., N.R. WIERSMA, D.J.R. WALSTRA, L.C. VAN RIJN, M.J.F. STIVE, 2004. Nourishing the shoreface: observations and hindcasting of the Egmond case, The Netherlands, *Coastal Engineering*, 51, pp. 813-837.
- VAN ENCKEVORT, I.M.J., 2001. Daily to yearly nearshore bar behaviour. PhD. Thesis, Utrecht Univ., 174 pp.
- VAN RIJN, L.C., 1993. Principles of sediment transport in rivers, estuaries and coastal seas, Aqua Publications, Oldemarkt.
- VAN RIJN, L.C., 1994. Principles of fluid flow and surface waves in rivers, estuaries, seas, and oceans, 2nd edition Aqua Publications, Oldemarkt.
- VAN RIJN, L.C., D.J.R. WALSTRA, B. GRASMEIJER, J. SUTHERLAND, S. PAN, J.P. SIERRA, 2003. The predictability of cross-shore bed evolution of sandy beaches at the time scale of storms and seasons using process-based Profile models, *Coastal Engineering*, 47, pp. 295-327.
- VAN RIJN, L.C. D.J.R. WALSTRA, 2003. Modelling of Sand Transport in Delft3D, WL | Delft Hydraulics report Z3624.
- VAN RIJN, L.C., D.J.R. WALSTRA, M. VAN ORMONDT, 2004. Description of TRANSPOR2004 and Implementation in Delft3D-ONLINE, Report Z3748.10, Delft Hydraulics.
- VAN RIJN, L.C., 2006a. A unified view of sediment transport by current and waves, Part I: Initiation of motion, ed roughness and bed load transport, *Journal of Hydraulic Engineering*, ASCE.
- VAN RIJN, L.C., 2006b. A unified view of sediment transport by current and waves, Part II: Suspended transport, *Journal of Hydraulic Engineering*, ASCE.
- VAN VOSSEN, B., 2000. Horizontal Large Eddy Simulations; evaluation of computations with DELFT3D-FLOW. Report MEAH-197, Delft University of Technology.
- WALSTRA, D.J.R., J.A. ROELVINK, J. GROENEWEG, 2000. Calculation of wave-driven currents in a 3D mean flow model. In: *Coastal Engineering 2000*, Billy Edge (ed.), Vol. 2, ASCE, New York, pp. 1050-1063.
- WIJNBERG, K.M., A. KROON, 2002. Barred beaches, *Geomorphology*, 48, pp. 103-120.
- WIJNBERG, K. M., J. H. J. TERWINDT, 1995. Extracting decadal morphological behaviour from high-resolution, long-term bathymetric surveys along the Holland coast using eigenfunction analysis, *Mar. Geol.*, 126, 301– 330.



WL | Delft Hydraulics

Rotterdamseweg 185
postbus 177
2600 MH Delft
telefoon 015 285 85 85
telefax 015 285 85 82
e-mail info@wldelft.nl
internet www.wldelft.nl

Rotterdamseweg 185
p.o. box 177
2600 MH Delft
The Netherlands
telephone +31 15 285 85 85
telefax +31 15 285 85 82
e-mail info@wldelft.nl
internet www.wldelft.nl

